Enhancing Wildfire Propagation Model Predictions Using Aerial Swarm-Based Real-Time Wind Measurements: A Conceptual Framework

Sadrabadi, M. T. & Innocente, M. S.

DOI 10.1016/j.apm.2024.03.012
ISSN 0307-904X
ESSN 1872-8480

Publisher: Elsevier

Applied Mathematical Modelling 130 (2024) 615–634

Contents lists available at ScienceDirect

Applied Mathematical Modelling

journal homepage: www.elsevier.com/locate/apm

Enhancing wildfire propagation model predictions using aerial swarm-based real-time wind measurements: A conceptual framework

Mohammad Tavakol Sadrabadi, Mauro Sebastián Innocente *

Autonomous Vehicles & Artificial Intelligence Laboratory, Coventry University, 7th Floor Friars House, Manor House Drive, Coventry, CV1 2TE, UK

ARTICLE INFO

Dataset link: https://github.com/AVAILab-org/Enhancing-wildfire-propagation-model-using-real-time-wind-measurements-AMM_2024

Keywords:
Wildland fire
Fire spread
Fire-induced wind
Fire–wind coupling
Wind downscaling
Unmanned aerial vehicles

ABSTRACT

The dynamic behaviour of wildfires is mainly influenced by weather, fuel, and topography. Based on fundamental conservation laws involving numerous physical processes and large scales, atmospheric models require substantial computational resources. Therefore, coupling wildfire and atmospheric models is impractical for high resolutions. Instead, a static atmospheric wind field is typically input into the wildfire model, either as boundary conditions on the control surface or distributed over the control volume. Wildfire propagation models may be (*i*) *data-driven*; (*ii*) *theoretical*; or (*iii*) *mechanistic surrogates*. Data-driven models are beyond the scope of this paper. Theoretical models are based on conservation laws (species, energy, mass, momentum) and are, therefore, computationally intensive; e.g. the Fire Dynamics Simulator (FDS). Mechanistic surrogate models do not closely follow fire dynamics laws, but related laws observed to make predictions more efficiently with sufficient accuracy; e.g. FARSITE, and FDS with the Level Set model (FDS-LS). Whether theoretical or mechanistic surrogate, these wildfire models may be coupled with or decoupled from wind models (e.g. Navier-Stokes equations). Only coupled models account for the effect of the fire on the wind field. In this paper, a series of simulations of wildfire propagation on grassland are performed using FDS-LS to study the impact of the fire-induced wind on the fire propagation dynamics. Results show that coupling leads to higher Rates of Spread (RoS), closer to those reported from field experiments, with increasing wind speeds and higher terrain slopes strengthening this trend. Aiming to capture the fire–wind interaction without the hefty cost of solving Navier-Stokes equations, a conceptual framework is proposed: 1) a swarm of unmanned aerial vehicles measure wind velocities at flight height; 2) the wind field is constructed with the acquired data; 3) the high-altitude wind field is mapped to near-surface, and 4) the near-surface wind field is fed into the wildfire model periodically. A series of simulations are performed using an in-house decoupled physics-based reduced-order fire propagation model (FireProM-F) enhanced by wind field "measurements". In this proof of concept, wind velocities are not measured but extracted from physics-based Large Eddy Simulations taken as ground truth. Unsurprisingly, higher measurement frequencies lead to more accurate and realistic predictions of the propagating fire front. An initial attempt is made to study the effect of wind measurement uncertainty on the model predictions by adding Gaussian noise. Preliminary results show that higher noise leads to the fire front displaying more irregular shapes and slower propagation.

* Corresponding author.
E-mail address: Mauro.S.Innocente@coventry.ac.uk (M.S. Innocente).
URL: https://availab.org (M.S. Innocente).

https://doi.org/10.1016/j.apm.2024.03.012
Received 11 September 2023; Received in revised form 11 February 2024; Accepted 18 March 2024

Available online 26 March 2024

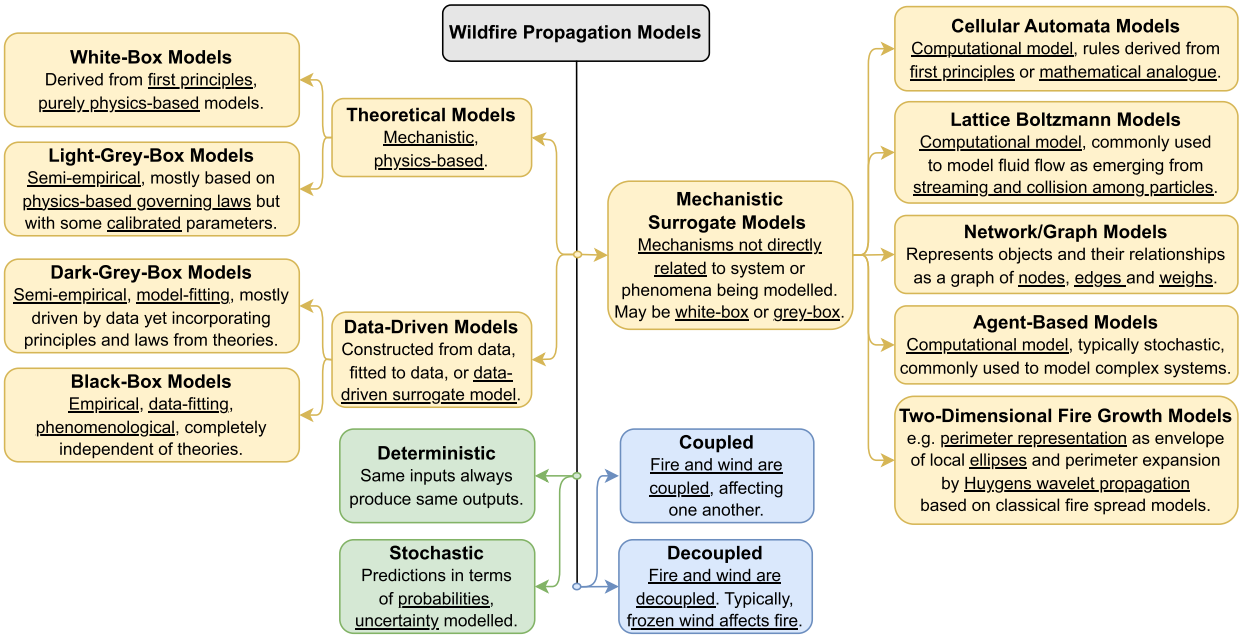

Fig. 1. Classification of fire propagation models. Modified from [7] to make it specific to wildfires and to explicitly differentiate coupled from decoupled models.

1. Introduction

The occurrence and behaviour of wildfires are greatly influenced by a combination of interrelated factors such as the ignition source, fuel composition and distribution, weather, and topography [1]. Wind—specifically, ground-level wind—is the most widely studied parameter involved in the fire–atmosphere interaction [2]. According to Gisborne [3], surface wind affects fire behaviour via four main mechanisms: (*i*) varying fuel moisture by carrying dry or humid air; (*ii*) varying the Rate of Spread (RoS) of the fire; (*iii*) carrying ignited branches or embers to unburned areas thus causing the ignition of spot fires; and (*iv*) bringing oxygen flux to the fire flame, thus boosting combustion.

Sullivan [4–6] classifies wildfire propagation models into three types: (*i*) *physical and quasi-physical* models, which are based on fundamental physics or chemistry of combustion [4]; (*ii*) *empirical and quasi-empirical* models, which are based on the statistical analysis of obtained data [5]; and (*iii*) *mathematical analogues and simulation* models, which are based on some mathematical conceit that coincidentally simulates the spread of fire [6]. Innocente and Grasso [7,8] classify them into three types (see Fig. 1, yellow boxes): (*i*) *theoretical* models, which are physics-based and involve conservation laws; (*ii*) *data-driven* models, which are constructed or fitted using actual or synthetic data; and (*iii*) *mechanistic surrogate* models, which make use of mechanisms not directly related to fire dynamics. In turn, Bakhshaii and Johnson [9] classify wildfire propagation models into three categories based on the level of their interaction with wind models: (*i*) *non-coupled*; (*ii*) *semi-coupled*; and (*iii*) *fully-coupled*. A wildfire model in which fire and wind models interact locally without being coupled with an atmospheric model would fall under the *semi-coupled* category. In this paper, we classify wildfire models into (*i*) *coupled* and (*ii*) *decoupled* depending on whether fire and wind models interact (see Fig. 1, blue boxes). This refers to the wildfire model alone, irrespective of whether it is coupled with an atmospheric model.

Seeking computational efficiency for operational use, models such as FARSITE [10] and the Fire Propagation Model for Fast simulations (**FireProM-F**) [8] are *decoupled* from wind models, neglecting the impact of the fire on the wind field. This increases epistemic uncertainty. FARSITE is a *mechanistic surrogate* model, which mainly relies on a simplified analytical calculation of the RoS and on Huygens' principle to approximate the propagation of the fire perimeter as if it were a wave front. FireProM-F [8,11] is a *theoretical* reduced-order model based on energy and species conservation laws with some calibrated physically-meaningful parameters (*light-grey-box* model). Despite being physics-based, it may run faster-than-real-time under certain circumstances (scenarios, settings, computing power), although this comes at the expense of being decoupled from wind models and therefore using a frozen wind field. While *decoupled* models may provide fast simulations of wildfire propagation [9], they are unable to capture structures such as plume-driven fire, whirls, or horizontal roll vortices [12].

Conversely, *coupled* models such as the Fire Dynamics Simulator (**FDS**) [13] and FIRETEC [14] attempt to solve the fluid dynamics and thermo-chemical equations simultaneously in order to capture the dynamics of a wildfire [9]. Even though some of these models (e.g. WRF-FIRE [15]) could potentially provide faster-than-real-time simulations under specific configurations and using high-performance facilities, an accurate numerical solution over a large domain is prohibitively computationally expensive [9]. This restricts the practical use of this type of models.

Even though the fire–wind coupling strategy significantly affects the simulation results, this is rarely studied systematically in the literature. Lopes et al. [16] studied the effects of the mesh size and of the wind update criterion on the fire propagation dynamics.

They found that the mesh size has a high impact on the RoS and propagation dynamics of the fire, though this impact becomes less noticeable as the mesh size decreases. Nevertheless, a truly mesh-independent simulation is unlikely to be achieved. In turn, comparing the results of a series of coupled and decoupled wildfire simulations, they observed that coupled ones predict significantly smaller burned areas. Interestingly, it was also found that reducing the wind field updates to once every five time-steps does not lead to significant variation in results, yet it notably reduces the computational effort [16]. Recently, Tavakol Sadrabadi et al. [17] also found that the burned area and the RoS are smaller for coupled simulations.

Thus, the choice of the right wildfire propagation model is highly dependent on the intended application: *coupled* models are more rigorous though computationally expensive (hence with limited operational use) whereas *decoupled* models decrease the computational cost at the expense of disregarding the effect of the fire on the wind field (hence sacrificing prediction accuracy). In order to compensate for this drawback, efforts have been made to increase the accuracy of the wind estimations; e.g. using Numerical Weather Prediction (NWP) models together with methods to downscale and refine these estimations over the terrain of interest [18]. However, these large-scale models cannot capture wildfires local effects.

During the past few years, Unmanned Aerial Vehicles (UAVs) have gained popularity in various industries and applications. They offer a low-cost option for firefighting, prevention, detection, and real-time assistance using either a single UAV or a collection of them [19,7,20]. Usually, UAVs (a.k.a. drones) are fitted with sensors that allow them to communicate with each other and to provide data to the ground station—e.g. GPS for navigation purposes [19], infrared and digital cameras for surveying and fire detection [21], and measuring sensors for aerosol concentrations [22] and wind velocities [22–25]. Firefighting activities largely depend on receiving accurate real-time data such as fire propagation characteristics, fuel distribution, and wind patterns. The availability of such data significantly increases the probability of success of the whole operation [26]. The use of drones in wildfire management has grown steadily in recent times, with most research focused on fire detection [27], monitoring [28], and suppression [29,30,7,31]. However, these drones could also be equipped with sensors to measure wind velocities while performing other tasks like fire monitoring and/or suppression. Therefore, this paper proposes a novel conceptual framework for improving the accuracy of *decoupled* wildfire propagation models using real-time wind field measurements carried out by a swarm of UAVs. As a proof of concept, these "*measurements*" are not actually taken by drones in the simulations performed in this paper but extracted from high-fidelity physics-based simulations viewed as ground truth. The proposed framework is mainly aimed at increasing the prediction accuracy of decoupled wildfire propagation models which disregard the effect of the fire on the wind field. However, it would also serve the purpose of capturing variable atmospheric wind on site without resorting to atmospheric models.

The remainder of this paper is organised as follows: Section 2 provides a brief overview of the main fire propagation models used in this research, namely FDS and its sub-models (Lagrangian Particle, Boundary Fuel, and Level Set), and FireProM-F; Section 3 discusses coupling strategies for fire–wind models and studies their impact on the RoS and fire propagation dynamics under different slopes and wind conditions using FDS-LS; Section 4 introduces the proposed method to improve the accuracy of decoupled wildfire propagation model predictions using real-time wind measurements carried out by a swarm of UAVs; whilst Section 5 presents the results obtained from simulations using FireProM-F with and without noise in the wind measurements; finally, Section 6 provides a summary of the research findings and derived conclusions.

2. Fire propagation models

This section presents a brief overview of the fire propagation models used for the simulations in this paper.

2.1. Fire dynamics simulator

The Fire Dynamics Simulator (**FDS**) numerically solves a variant of the Navier-Stokes equations suitable for low-speed, thermally-driven flow with a focus on smoke and heat transfer from fires. The main algorithm includes an explicit predictor-corrector method that is second-order accurate in space and time. Turbulence is modelled via Large Eddy Simulations (LES). A Direct Numerical Simulation (DNS) could be carried out instead, should the mesh be sufficiently fine. FDS employs a one-step, mixing-controlled chemical reaction with three bundled species for most applications: *products*, *fuel*, and *air*. Reactions that are not necessarily mixing-controlled and multiple reactions could also be considered under certain conditions. To approximate the governing equations and discretise the domain, a Cartesian grid is used [32]. FDS offers various models for the simulation of wildfire spread based on the desired level of physics required and the available computing resources: the Lagrangian Particle Model (LPM), the Boundary Fuel Model (BFM), and the Level-Set (LS) model. In this paper, FDS 6.7.9 is used for the simulations.

2.1.1. Lagrangian particle model

In this model, vegetation is represented by a collection of Lagrangian particles heated via convection-radiation heat transfer. These particles may be used to represent leaves, grass, trees, etc. With sufficient grid refinement, LPM can be used for simulation of the front, back, and flank fire across the surface as well as high-level vegetations (e.g. trees) [33].

2.1.2. Boundary fuel model

This model is suitable when a coarse grid is desired to discretise a thin vegetation layer. Vegetation is modelled as a porous boundary consisting of a layer of dry vegetation, air, and moisture. The height of the vegetation is unresolved on the grid and may be used for grid sizes of up to 10 m [32,33].

2.1.3. Level set model

This model is used for wildfires propagating across large areas, which cannot be discretised with a grid sufficiently fine for physics-based models. FDS with the Level Set model (**FDS-LS**) uses the same elliptical spread model used by FARSITE [10,34], which is based on Huygens' principle for wave propagation modelling. It also adopts Rothermel-Albini's RoS formula and Albini's 13 fuel models [32]. The meaning of the font colours of some variables will be explained towards the end of this section.

A series of parameters must be set to define a fuel in FDS-LS, including the no-wind no-slope rate of spread $\left(RoS_0\right)$ for unburned fuel, the packing ratio (β), the surface area-to-volume ratio (σ), and the fuel height (h). These settings are used to calculate the mid-flame wind velocity $\left(\mathbf{u}_{\mathrm{mf}}\right)$ and the wind and slope coefficients ($\boldsymbol{\phi}_{\mathrm{w}}$ and $\boldsymbol{\phi}_{\mathrm{s}}$, respectively). Since wind and slope are generally not aligned with each other or with the direction of the fire spread, they are both coefficient vectors [35,34]:

$$\boldsymbol{\phi}_{\mathrm{w}} = \left(\phi_{\mathrm{w},x}, \phi_{\mathrm{w},y}\right) = C\,(3.281)^{B} \left(\frac{\beta}{\beta_{\mathrm{op}}}\right)^{-E} \cdot \left(\left|u_{\mathrm{mf},x}\right|^{B} \operatorname{sgn}\left(u_{\mathrm{mf},x}\right), \left|u_{\mathrm{mf},y}\right|^{B} \operatorname{sgn}\left(u_{\mathrm{mf},y}\right)\right) \tag{1}$$

$$\boldsymbol{\phi}_{\mathrm{s}} = \left(\phi_{\mathrm{s},x}, \phi_{\mathrm{s},y}\right) = 5.275\ \beta^{-0.3} \left(\left(\frac{\Delta z}{\Delta x}\right)^{2}, \left(\frac{\Delta z}{\Delta y}\right)^{2}\right) \tag{2}$$

with

$$B = 0.15988\ \sigma^{0.54} \tag{3}$$

$$C = 7.47\ \mathrm{e}^{-0.8711\ \sigma^{0.55}} \tag{4}$$

$$E = 0.715\ \mathrm{e}^{-0.01094\ \sigma} \tag{5}$$

$$\beta_{\mathrm{op}} = 0.20395\ \sigma^{-0.8189} \tag{6}$$

$$\mathbf{u}_{\mathrm{mf}} = \left(u_{\mathrm{mf},x}, u_{\mathrm{mf},y}\right) = \mathbf{u}_0 \frac{1.83}{\ln\left(\frac{20+1.18\ h}{0.43\ h}\right)} \tag{7}$$

where $\mathbf{u}_0$ is the wind velocity at 6.1 m Above Ground Level (AGL), and h is the fuel height in meters. FDS-LS calculates $\mathbf{u}_0$ by dividing $\mathbf{u_{10}}$ (wind velocity at 10 m AGL) by 1.15, with $\mathbf{u_{10}}$ defined by the user as a boundary condition (input).

The surface RoS is obtained following Rothermel's model using the magnitude of the combined wind and slope coefficient vectors as in Equation (8) [34]:

$$RoS = RoS_0 \left(1 + \sqrt{\left(\boldsymbol{\phi}_{\mathrm{w}} + \boldsymbol{\phi}_{\mathrm{s}}\right) \cdot \left(\boldsymbol{\phi}_{\mathrm{w}} + \boldsymbol{\phi}_{\mathrm{s}}\right)}\right). \tag{8}$$

FDS-LS assumes that, under specific wind, slope, and vegetation circumstances, a surface fire will spread from a single ignition point with an ellipse-shaped fire perimeter that has a constant length-to-breadth (LB) ratio for the effective wind velocity $\left(\mathbf{u}_{\mathrm{eff}}\right)$ [32]. The latter is defined as:

$$\mathbf{u}_{\mathrm{eff}} = \mathbf{u}_0 + \mathbf{u}_{\mathrm{vir}} \tag{9}$$

where $\mathbf{u}_{\mathrm{vir}}$ is the virtual wind velocity aimed at accounting for the effect of slope [10]:

$$\mathbf{u}_{\mathrm{vir}} = 0.3048 \left(\frac{1}{c}\left(\frac{\beta}{\beta_{\mathrm{op}}}\right)^{E}\right)^{\frac{1}{B}} \boldsymbol{\phi}_{\mathrm{s}}. \tag{10}$$

Thus, the effective wind velocity $\left(\mathbf{u}_{\mathrm{eff}}\right)$ combines the prescribed wind velocity $\left(\mathbf{u}_0\right)$ and the effect of slope $\left(\mathbf{u}_{\mathrm{vir}}\right)$.

Let $P(t)$ be a point on the fire front at time t. The LB ratio for the elliptical fire front originating from $P(t)$ is as in Equation (11) [10,34]:

$$LB = \max\left(1, \min(\overline{LB}, 8)\right) \tag{11}$$

where

$$\overline{LB} = 0.936\ \mathrm{e}^{0.2566\ u_{\mathrm{eff}}} + 0.461\ \mathrm{e}^{-0.1548\ u_{\mathrm{eff}}} - 0.397 \tag{12}$$

and $u_{\mathrm{eff}} = \|\mathbf{u}_{\mathrm{eff}}\|$ is the effective wind speed.

The heading-to-backing ratio (HB), which is the ratio of the fire propagation in the wind direction to its propagation in the opposite direction, is given by [10,34]:

$$HB = \left(LB + \sqrt{LB^2 - 1}\right)\left(LB - \sqrt{LB^2 - 1}\right)^{-1}. \tag{13}$$

Let $P(t + \mathrm{d}t)$ be a point on the fire front at time $(t + \mathrm{d}t)$. Its location is obtained by modelling the fire propagation from $P(t)$ as an ellipse with semi-minor and semi-major axes ($a\ \mathrm{d}t$) and ($b\ \mathrm{d}t$), respectively, where:

$$a = \frac{b}{LB} \quad \text{and} \quad b = \frac{1}{2}\left(RoS + \frac{RoS}{HB}\right). \tag{14}$$

Note that a and b are the rates of spread corresponding to the semi-axes of the ellipse, while RoS is as in Equation (8). The distance between $P(t)$ and the centre of the ellipse is given by $(c\ \mathrm{d}t)$, where:

$$c = b - \frac{RoS}{HB}. \tag{15}$$

Thus, the components of the RoS in the axes of the computational grid are calculated as follows:

$$RoS_x = D\left[a^2 \cos\theta \left(x_s \sin\theta + y_s \cos\theta\right) - b^2 \sin\theta \left(x_s \cos\theta - y_s \sin\theta\right)\right] + c \sin\theta \tag{16}$$

$$RoS_y = D\left[-a^2 \sin\theta \left(x_s \sin\theta + y_s \cos\theta\right) - b^2 \cos\theta \left(x_s \cos\theta - y_s \sin\theta\right)\right] + c \cos\theta \tag{17}$$

where

$$D = \left[a^2 \left(x_s \sin\theta + y_s \cos\theta\right)^2 + b^2 \left(x_s \cos\theta - y_s \sin\theta\right)^2\right]^{-\frac{1}{2}}, \tag{18}$$

the quantities x_s and y_s are related to the components of the vector normal to the elliptical fire front, and θ is the clockwise angle between the y-axis of the computational grid and the direction of the maximum spread as a function of the local wind, terrain, and vegetation [34]:

$$\theta = \mathrm{atan2}\left[\left(\phi_{w,y} + \phi_{s,y}\right) + \left(\phi_{w,x} + \phi_{s,x}\right)\right]. \tag{19}$$

Thus, this model predicts the propagation of the fire front (assuming it behaves like a wave) affected by the wind and the terrain slope. It is a *decoupled model* (see Fig. 1), since the fire does not affect the wind field. The same is true for FARSITE [10]. Therefore, the conceptual framework proposed in this paper for improving the accuracy of *decoupled* wildfire propagation models using real-time wind field measurements carried out by a swarm of UAVs could be applied. In order to do so, the wind velocity at 6.1 m $(\mathbf{u}_0)$ shown in blue is to be measured. (For interpretation of the colours, the reader is referred to the web version of this article.) This affects the mid-flame wind velocity $(\mathbf{u}_{mf})$ shown in violet, which in turn affects the wind coefficient $(\boldsymbol{\phi}_w)$ shown in red and therefore the RoS and the orientation of the ellipse (θ). The effective wind velocity $(\mathbf{u}_{eff})$ shown in violet is also affected by $\mathbf{u}_0$, affecting *LB* and *HB*, and therefore the shape of the ellipse.

However, the LS model within FDS may be coupled with its wind model, thus becoming a *coupled model*—albeit not fully physics-based. We make use of this capability of FDS-LS to study the effect of fire–wind coupling in Section 3. To this end, the combustion model must also be coupled. Thus, when the fire reaches a surface cell, fuel vapours are generated at a constant rate $(\dot{m}''_f)$ [32]:

$$\dot{m}''_f = (1 - \nu_{char})\frac{m''_f}{\delta_t}\left[\frac{\mathrm{kg}}{\mathrm{m}^2\ \mathrm{s}}\right], \text{ where } \delta_t = \frac{75,600}{\sigma}[\mathrm{s}] \tag{20}$$

is the duration of the burn at a given location, ν_{char} is the char fraction (0.2 by default), and m''_f is the dry fuel loading $\left[\mathrm{kg/m^2}\right]$.

Coupling the LS fire propagation model with the wind model results in FDS-LS accounting for terrain-induced wind fields as well as fire–wind interaction by presenting a simple heat source at the fire front location [34]. Thus, FDS-LS may be used in any of four modes:

- Mode 1: Wind field is uniform and unaffected by terrain or fire (frozen uniform wind field). Only the fire model runs. Fire affected by frozen wind. According to Fig. 1, this is a *decoupled* wildfire model.
- Mode 2: Wind field affected by terrain but unaffected by fire (frozen non-uniform wind field). Fire affected by frozen wind. According to Fig. 1, this is a *decoupled* wildfire model.
- Mode 3: Wind field follows terrain but there is no actual fire in the simulation (just front-tracking) [32].
- Mode 4: Wind field affected by terrain and fire. Fire affected by wind. According to Fig. 1, this is a *coupled* wildfire model.

Readers are kindly referred to [34] for a more detailed description of FDS-LS. The literature on FARSITE [10] is also helpful to understand the approach of modelling fire propagation using Huygens' principle.

2.2. Fire propagation model for fast simulations

The physics-based **Fire Pro**pagation **M**odel for **F**ast simulations (**FireProM-F**) [8] is a wildfire model developed with computational efficiency in mind, aiming for faster-than-real-time (FtRT) simulations. It is governed by a 2D reaction-diffusion equation that describes the combustion of a vegetation stratum represented by a mono-phase medium composed of pre-mixed gas of fuel and air. The fuel is assumed to be methane (after pyrolysis) whilst the air is assumed to be composed of oxygen, carbon dioxide, water vapour, and nitrogen. The reference chemical reaction (assumed irreversible) is the combustion of methane in air:

$$\theta_1 CH_4 + \theta_2 O_2 \rightarrow \theta_3 CO_2 + \theta_4 H_2O \quad \left(\text{in air: } \theta_5 N_2\right). \tag{21}$$

The model is formulated as a system of five partial differential equations (PDEs), where Equation (22) represents the conservation of energy whilst the four equations in (23) represent the conservation of chemical species.

$$\rho\frac{\partial}{\partial t}\left(c_{\mathrm{p}}T\right)=R_{\mathrm{c}}-\nabla\cdot\left(\mathbf{q}_{\mathrm{c}}+\mathbf{q}_{\mathrm{d}}+\mathbf{q}_{\mathrm{r}}\right)+Q_{\mathrm{cz}}+Q_{\mathrm{rz}}+Q_{\mathrm{w}} \tag{22}$$

$$\frac{\partial X_i}{\partial t}=-\frac{\theta_i}{\theta_1}\frac{M_i}{M_1}r;\quad \text{with } i=1,2,3,4, \tag{23}$$

where

T: temperature;
ρ: mass density;
c_{p}: specific heat capacity of the mixture;
R_{c}: combustion energy;
X_i: mass fraction of i^{th} chemical species;
M_i: molar mass of i^{th} chemical species;
r: combustion rate;
$\mathbf{q}_{\mathrm{c}}$: conductive heat flux;
$\mathbf{q}_{\mathrm{d}}$: interdiffusional enthalpy flux;
$\mathbf{q}_{\mathrm{r}}$: 2D radiation heat flux;
Q_{cz}: vertical convection heat loss;
Q_{rz}: vertical radiation heat loss;
Q_{w}: transport term due to wind.

The specific heat capacity of the mixture is given by

$$c_{\mathrm{p}}=\sum_{i=1}^{5}X_i\frac{M_i}{M}c_{\mathrm{p}i}, \tag{24}$$

where the molar mass of the mixture is a linear combination of the molar masses of each chemical species multiplied by their respective mass fraction:

$$M=\sum_{i=1}^{5}X_iM_i. \tag{25}$$

The combustion energy is given by

$$R_{\mathrm{c}}=-\rho c_{\mathrm{h}}h_{\mathrm{c}}\frac{M}{M_1}r \tag{26}$$

where h_{c} is the combustion enthalpy, and c_{h} is the enthalpy proportionality coefficient. The latter accounts for the possibility of burning fuels which have different R_{c} than that of methane. The combustion rate (r) follows Arrhenius law:

$$r=-\delta^{+}_{(T,X_{1,2})}A_rTX_1^{0.5}X_2\exp\left(-\frac{T_{\mathrm{a}}}{T}\right) \tag{27}$$

where A_r is the pre-exponential coefficient and T_{a} is the activation temperature, which are empirical parameters that depend on the fuel structural and chemical properties. In turn, the Kronecker delta stands for the extinction model:

$$\delta^{+}_{(T,X_{1,2})}=\begin{cases}1 & \text{if}\quad T>T_{\mathrm{ig}}\wedge X_{1,2}>X_{1,2\mathrm{e}}\\ 0 & \text{otherwise}\end{cases} \tag{28}$$

where T_{ig} is the ignition temperature (assumed to be the same as T_{a}), while $X_{1\mathrm{e}}$ and $X_{2\mathrm{e}}$ are the flame extinction values of the fuel and oxidant mass fractions, respectively. The combustion enthalpy is the summation of all formation enthalpies $\left(H_i\right)$ at the specific local T:

$$h_{\mathrm{c}}=\frac{H_{\mathrm{c}}(T)}{M}=-\frac{1}{M}\sum_{i=1}^{5}\theta_iH_i(T)$$

$$h_{\mathrm{c}}=\frac{1}{M}\sum_{i=1}^{5}\theta_i\left[H_{i,\mathrm{ref}}+M_ic_{\mathrm{p}i}\left(T_{\mathrm{ref}}-T\right)\right] \tag{29}$$

where the reference empirical values $H_{i,\mathrm{ref}}$ and T_{ref} can be found in [36].

The conductive heat flux is given by

$$\mathbf{q}_{\mathrm{c}}=-\kappa\nabla T, \tag{30}$$

where the thermal conductivity (κ) is considered constant. In turn, the interdiffusional enthalpy flux is approximated by

$$\mathbf{q}_{\mathrm{d}} \approx \frac{\kappa T}{c_{\mathrm{p}} M} \sum_{i=1}^{5} c_{\mathrm{p}i} \nabla \left(X_i M_i \right) \tag{31}$$

while the 2D radiation heat flux is approximated by

$$\mathbf{q}_{\mathrm{r}} \approx -4\sigma\varepsilon\delta_x T^3 \nabla T \tag{32}$$

where σ is the Boltzmann constant, ε is the emittance, and δ_x is the absorption length (a.k.a. optical thickness). The latter is assumed to be isotropic, and it must not be larger than the smallest cell size for the numerical solution to be valid.

With this dimensionality reduction, some fire dynamics phenomena like buoyancy are disregarded. Nonetheless, vertical convection (Q_{cz}) and vertical radiation (Q_{rz}) terms are added to the conservation of energy equation in (22), with:

$$\begin{aligned} Q_{\mathrm{cz}} &= \chi \left(T_{\mathrm{amb}} - T \right) \\ Q_{\mathrm{rz}} &= \sigma\varepsilon\delta_z^{-1} \left(T_{\mathrm{amb}}^4 - T^4 \right) \end{aligned} \tag{33}$$

where T_{amb} is the ambient temperature, χ is the convection coefficient, and δ_z is the vertical optical thickness.

FireProM-F does not account for conservation of mass or momentum, thus neglecting the effect of the fire on the wind field. The diffusion coefficient is augmented (via calibration) to compensate for this. Refer to [8] for more details.

The transport term due to wind (Q_{w}) in Equation (22) is calculated as in Equation (34):

$$Q_{\mathrm{w}} = -\rho\, c_{\mathrm{w}}\, \mathbf{u} \cdot \nabla \left(c_{\mathrm{p}}\, T \right) \tag{34}$$

where $\mathbf{u} = (u_x, u_y)$ is the atmospheric wind velocity, and c_{w} is the wind reduction coefficient (which may also be used for calibration).

The numerical scheme for the solution of Equations (22) and (23) is a finite difference method with a 2nd-order central difference for space and the 4th-order Runge-Kuta method for time discretisations. Refer to [8] for the full formulation.

This reduced-order model, FireProM-F, is adopted in this paper as a fast yet still physics-based simulator to test the proposed framework. The latter aims to enhance the accuracy of the transport term (Q_{w}) by feeding the model with wind velocities ($\mathbf{u}$) measured by a swarm of UAVs. While the main purpose is to account for the effect of the fire on the wind field, it also serves the purpose of accounting for variable atmospheric wind.

2.3. Calibration and validation

2.3.1. Experimental data

Numerical simulations are validated against flat terrain grassland fire spread experiments carried out by the Commonwealth Scientific and Industrial Research Organisation (CSIRO) [37,38]. As in [13], C064 and F19 are the selected experiments, which were performed in the middle of the dry season on flatlands of 100×100 m^2 covered with dry Kerosene grass and of 200×200 m^2 covered with dry Kangaroo grass, respectively. During each experiment, the reference wind speed (u_{r}) was measured at 2 m AGL whereas the air temperature $\left(T_{\mathrm{amb}}\right)$ and relative humidity were measured at 1.4 m AGL. Fuel load $\left(m_{\mathrm{f}}''\right)$ and height (h) were sampled at different locations and averaged within each plot. Other fuel characteristics, including surface area-to-volume ratio (σ) and fuel moisture content (FMC), were also measured and recorded. Two workers ignited fires, starting at the midpoint and moving towards either side of the plot. The length of ignition is around 50 m for 100×100 m^2 plots and around 175 m for 200×200 m^2 plots. Fire behaviour was then studied through data gathered by ground observations and oblique aerial photographs. The RoS was calculated for each experiment as the maximum distance travelled by the fire between successive time steps. Measured properties during the experiments in [38] are presented in Table 1 along with unmeasured properties assumed or adopted from other studies in [33].

It is worth noting that there are different sources of uncertainty in the experiments. For C064, wind speed in the x-direction at each corner of the field was measured every 5 s, exhibiting high variability. Furthermore, the fuel load was sampled at different locations and averaged over the field for the simulations. A thorough study of uncertainties brought about by measurements, simplifications, and assumptions, and their impact on the results of field and numerical experiments, is beyond the scope of this paper.

2.3.2. Boundary conditions and grid sensitivity

Open boundary conditions are used at the top, outlet, right, and left boundaries. Ambient wind is simulated using Monin-Obukhov similarity theory, with Obukhov length $L = -500$ m, aerodynamic roughness length $z_0 = 0.03$ m, $u_{\mathrm{r}} = 4.6$ m/s for C064, and $u_{\mathrm{r}} = 4.8$ m/s for F19.

Structured Cartesian grids with equal spacing in x, y, z directions are used to discretise a $120 \times 120 \times 40$ m^3 domain for C064 and a $240 \times 240 \times 100$ m^3 domain for F19. In order to study the sensitivity of the simulated fire propagation to the grid cell size, sizes between $1 \times 1 \times 1$ m^3 and $5 \times 5 \times 5$ m^3 are tested using FDS-LS, and sizes of $0.5 \times 0.5 \times 0.5$ m^3 and $1 \times 1 \times 1$ m^3 are tested using FDS-LPM and FDS-BFM.

FDS-LS uses Albini's fuel models [32] by default, which sets the values of h, σ, β, ν_{char}, m_{f}'', and RoS_0 for different pre-defined fuel types. Following [33] and as a first step, Albini's fuel type 1 (*short grass*) and fuel type 3 (*tall grass*) are used here to represent the fuel in C064 and F19 experiments, respectively. The evolution of the fire front is shown in Fig. 2 for both experiments, cell sizes of 1 m, 2 m, 3 m and 5 m, and both *coupled* (C) and *decoupled* (D) configurations. It can be observed that the predicted fire front is sensitive to both cell size and fire–wind coupling. The C-configuration predicts higher RoS, which is closer to the experimental results. Increasing cell size generally leads to higher RoS as well, in agreement with results in [33].

Table 1
Measured properties of CSIRO experiments [38] and settings for simulations based on [13,33].

Property	Unit	Case C064	Case F19	Reference
Reference Wind Speed (u_r)	m/s	4.6	4.8	[37]
Ambient Temperature (T_{amb})	°C	32	34	[37]
Surface Area to Volume Ratio (σ)	m^{-1}	9,770	12,240	[37]
Grass Height (h)	m	0.21	0.51	[37]
Fuel load (m''_f)	kg m^{-2}	0.283	0.313	[37]
Fuel moisture content	%	6.3	5.8	[37]
Measured RoS	m s^{-1}	1.2	1.5	[37]
Fuel	-	Cellulose ($C_6H_{10}O_5$)	Cellulose ($C_6H_{10}O_5$)	Assumed [33]
Heat of Combustion (H_c)	kJ kg^{-1}	15,600	15,600	[33]
Soot Yield (ν_{soot})	kg kg^{-1}	0.015	0.015	[33]
Char Yield (ν_{char})	kg kg^{-1}	0.2	0.2	[33]
Specific Heat	kJ kg^{-1} K^{-1}	1.5	1.5	Assumed [33]
Conductivity	kJ kg^{-1} K^{-1}	0.1	0.1	Assumed [33]
Density (ρ)	kg m^{-3}	512	512	[33]
Heat of Pyrolysis	kJ kg^{-1}	418	418	[33]
Pyrolysis Temperature	°C	200	200	[33]
Obukhov Length (L)	m	−500	−500	Assumed [33]
Aerodynamic Roughness Length (z_0)	m	0.03	0.03	Assumed [33]
Drag Coefficient (c_d)	-	2.8	2.8	[33]
Soil Specific Heat	kJ kg^{-1} K^{-1}	2.0	2.0	[33]
Soil Conductivity	W m^{-1} K^{-1}	0.25	0.25	[33]
Soil Density	kg m^{-3}	1,300	1,300	[33]
Relative Humidity	%	40	40	Assumed [33]

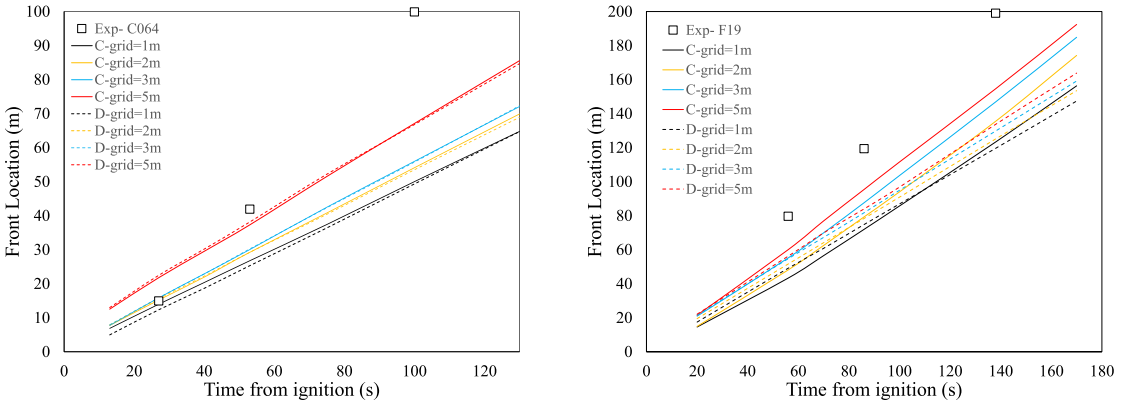

(a) Albini's type 1 fuel model, CSIRO C064.

(b) Albini's type 3 fuel model, CSIRO F19.

Fig. 2. Evolution of simulated fire front location predicted by FDS-LS for CSIRO C064 and F19 experiments using Albini's fuel models, cell sizes of 1 m, 2 m, 3 m and 5 m, and both *coupled* (C) and *decoupled* (D) configurations. Results from field tests are also provided for reference.

FDS-LPM and FDS-BFM incorporate pyrolysis and combustion models. Using the settings in Table 1, Fig. 3 shows the evolution of the fire front location predicted by FDS-LPM and FDS-BFM for the C064 and F19 experiments with cell sizes of 0.5 m and 1 m. The predicted RoS is higher than the experimental values, with the smaller cell size providing better predictions. A thorough sensitivity analysis of the model parameters is beyond the scope of this paper. The differences in predictions may be due to a range of inaccurate settings such as those of the LES turbulence model parameters, fuel properties (e.g. ν_{char}, c_d), and other thermogravimetric vegetation properties defined in the model, yet not measured during the field experiments.

2.3.3. *FDS-LS fuel definition and RoS_0 calibration*

Although FDS-LS uses Albini's fuel models [32] by default, it is possible to define other fuels. Since the predicted fire front locations in Fig. 2 do not accurately match the experimental results, a custom fuel type is defined with the physical characteristics in Table 1 to represent the Kangaroo grass in the CSIRO F19 field experiment. This experiment is chosen here due to its larger domain, which is more convenient to study the effect of the fire–wind coupling in Section 3. Since FDS-LS does not require the thermal properties of the vegetation, only h, σ, β, ν_{char}, and m''_f are required from Table 1, with RoS_0 being calibrated.

Calibration is carried out for three cell sizes and coupled FDS-LS (Mode 4). Fig. 4 (a) shows that the evolution of the fire front location now matches the field measurements, with the calibrated RoS_0 only marginally larger than that of Albini's fuel type 3 (*tall grass*). Fig. 4 (b) shows the predicted fire perimeter of the simulated fire predicted by the coupled FDS-LS with calibrated RoS_0 for cell sizes of 2 m, 3 m and 5 m at three time instances since ignition.

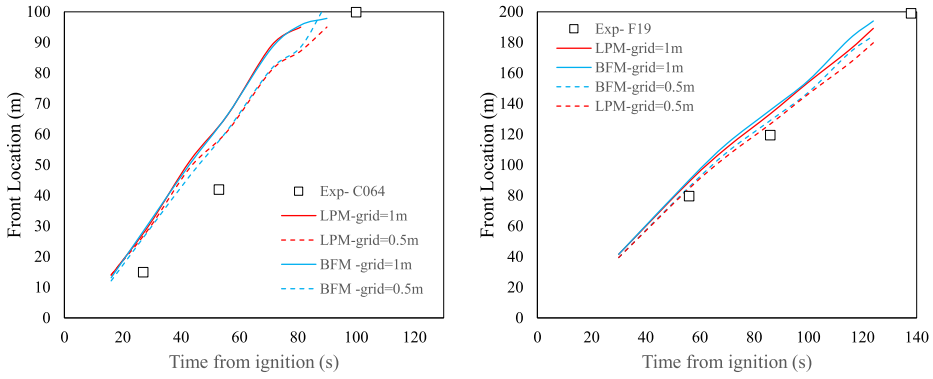

(a) Custom fuel type as in Table 1, CSIRO C064.

(b) Custom fuel type as in Table 1, CSIRO F19.

Fig. 3. Evolution of simulated fire front location predicted by FDS-LPM and FDS-BFM (including pyrolysis and combustion models) for CSIRO C064 and F19 experiments using cell sizes of 0.5 m and 1 m, and settings as in Table 1. Results from field tests are also provided for reference.

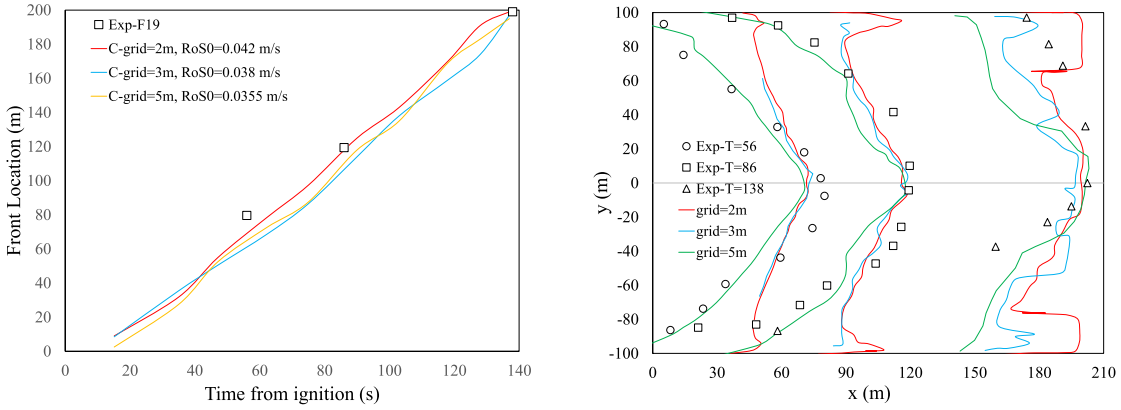

(a) Evolution of simulated fire front location.

(b) Fire perimeter at 56 s, 86 s and 138 s since ignition.

Fig. 4. (a) Evolution of simulated fire front location and (b) fire perimeter at three time instances since ignition, as predicted by coupled FDS-LS for CSIRO F19 experiment using custom fuel type defined by physical characteristics in Table 1, calibrated RoS_0, and cell sizes of 2 m, 3 m and 5 m. Results from field test are also provided for reference.

3. Coupling strategies for fire–wind models

Fig. 4 (b) shows that the coupled FDS-LS with calibrated RoS_0 accurately predicts the CSIRO F19 experiment under no-slope conditions. The effects of fire–wind coupling on the headfire position and the resulting RoS for a range of wind speeds and topography slopes during upslope propagation with the same custom fuel can be observed in Fig. 5, where $2 \times 2 \times 1$ m^3 cells are used for spatial discretisation. Given that FDS uses structured grids, a sloped topography is modelled using a staircase of cubic blocks.

Fig. 5 shows (a) the headfire position (distance travelled) and (b) corresponding RoS for eight wind speeds in the range of 1–20 m/s and horizontal topography. It also shows (c) the head fire position and (d) corresponding RoS for a fire propagating upslope for all nine possible combinations of three slopes (5%,15%, 30%) and three wind speeds (1 m/s, 5 m/s, 10 m/s). Both *coupled* (C) and *decoupled* (D) FDS-LS are used to model each scenario. Note that *wind speed* refers to horizontal reference wind speed (u_r), whilst the resulting upslope wind speed is higher. As expected, higher wind speed and higher topography slope (for upslope propagation) lead to higher RoS. Furthermore, higher wind speeds of up to 10 m/s and higher surface slopes of up to 30% also result in larger differences between predictions by corresponding coupled and decoupled fire–wind models, in agreement with experimental results in [39]. For example, the difference between coupled and decoupled predictions of the RoS is 0.44 m/s for 30% slope and 5 m/s wind, whereas it is 1.51 m/s for 30% slope and 10 m/s. The RoS predicted by coupled FDS-LS appears to be generally higher than the one predicted by its decoupled counterpart for wind speeds of up to 12 m/s. For horizontal topography in Fig. 5 (b), this trend seems to invert for wind speeds approximately between 12 m/s and 20 m/s, with the coupling strategy making little to no difference for a wind speed of 20 m/s. More data points would be required to analyse this observation.

It is important to note that these simulations using FDS-LS suggest that increasing wind speeds always leads to increasing RoS. However, experimental results [2,40] showed that a turning point and a reduction of the RoS is to be expected. In fact, the model tends to overestimate the RoS for increasing wind speeds when compared to typical values reported in the literature, especially for extreme cases—in which model predictions are counter-intuitive. Since FDS-LS is not physics-based, it is reasonable to infer that

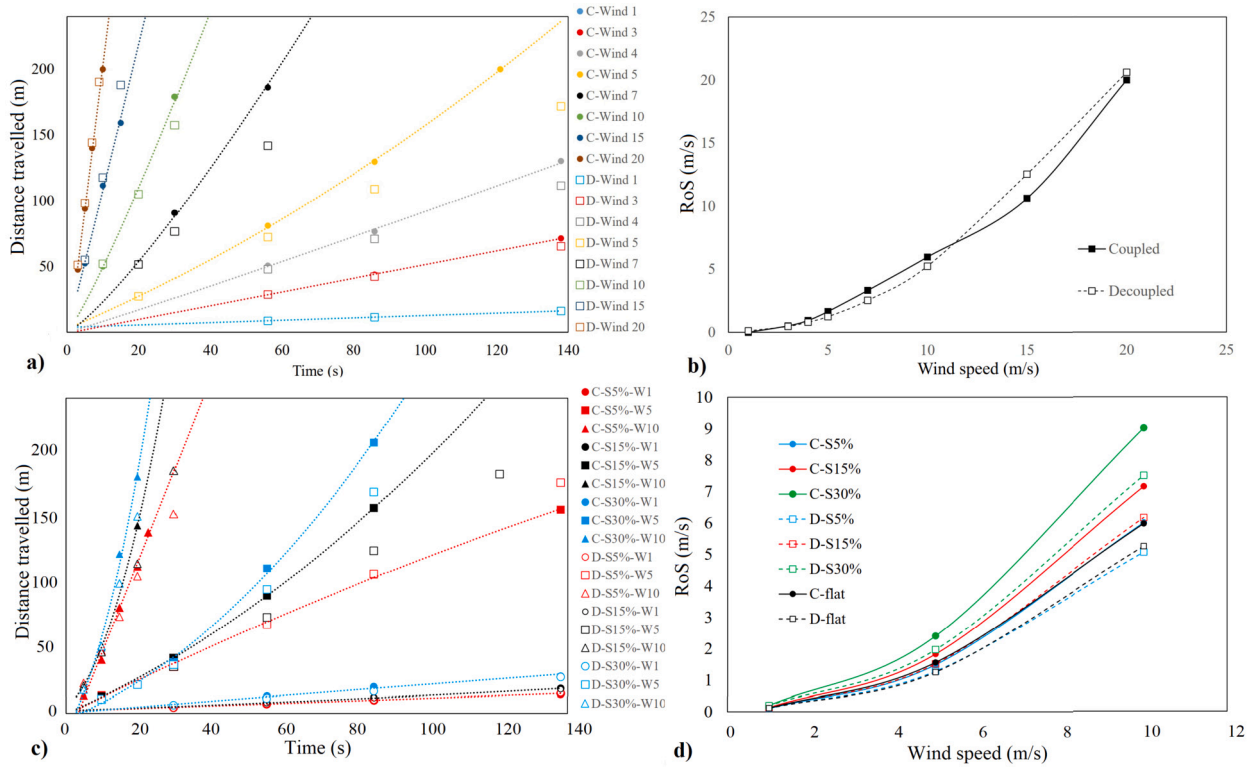

Fig. 5. (a) Headfire position for eight wind speeds in the range of 1–20 m/s and (b) their corresponding RoS for horizontal topography; and (c) headfire position for nine slope–wind combinations in the range of 1–10 m/s and 5–30% and (d) their corresponding RoS with fire propagating upslope. Both *coupled* (C) and *decoupled* (D) FDS-LS are used to model each scenario.

it does not capture some of the relevant underlying fire propagation dynamics, and therefore may make unreliable predictions for higher wind speeds (here, higher than ≈10–12 m/s).

Wildfires can propagate upslope surprisingly fast due to the preheating of unburned fuel ahead of the fire as the plume attaches to the slope surface [41]. Under no-wind no-slope conditions, fuel preheating is governed largely by radiation, since upstream and downstream air entrainment is the same, hence forming a vertical uprising plume. As the angle between the fire plume and the fuel bed shrinks, the length of the plume attachment increases, resulting in a higher RoS. This angle shrinks as the *flame tilt angle* (θ) and the *fuel bed inclination angle* (α) increase, where θ is the angle between the centerline of the individually pioneering flame and the vertical axis [42]. In turn, θ increases with increasing upslope *wind speed* and with increasing α due to the resulting asymmetric *air entrainment*. Since buoyancy has an upslope component, air entrainment into the fire from the burned side (upstream) is greater, hence tilting the plume towards the unburned downstream vegetation [43]. Therefore, higher upslope *wind speeds* and higher *surface slopes* lead to faster upslope fire propagation due to the resulting larger *plume attachment length*. Even though FDS-LS does not model the flame, radiative heat transfer, or fuel preheating effects, the larger RoS predicted for larger surface slopes when coupling fire and wind models during upslope fire propagation is likely due to the released latent heat from the fire front, which contributes to the formation of convective wind patterns upslope.

Thus, higher wind speeds and larger inclinations of the fuel bed result in faster upslope fire propagation. Coupled FDS-LS predicts faster propagation than its decoupled counterpart, presumably better capturing the relevant phenomena associated with fire–induced wind. Fig. 6 also shows that decoupled FDS-LS displays smoother perimeters.

4. Enhancement for decoupled models

In Section 3, the influence of the fire on the wind field has been shown to have a strong effect on its RoS, and therefore should not be neglected when predicting its propagation. Yet, this is precisely what decoupled wildfire models do. Aiming to capture the fire–wind interaction without incurring the hefty cost of solving the Navier-Stokes equations, a methodology is proposed to enhance wildfire model predictions by providing it with near-surface wind fields approximated from UAV measurements at higher altitudes.

4.1. System overview

The proposed methodology is model agnostic, and therefore can be implemented as a stand-alone module to be integrated with any wildfire model that includes wind in its governing equations. Since its aim is to mimic the effect of fire–wind coupling, it is

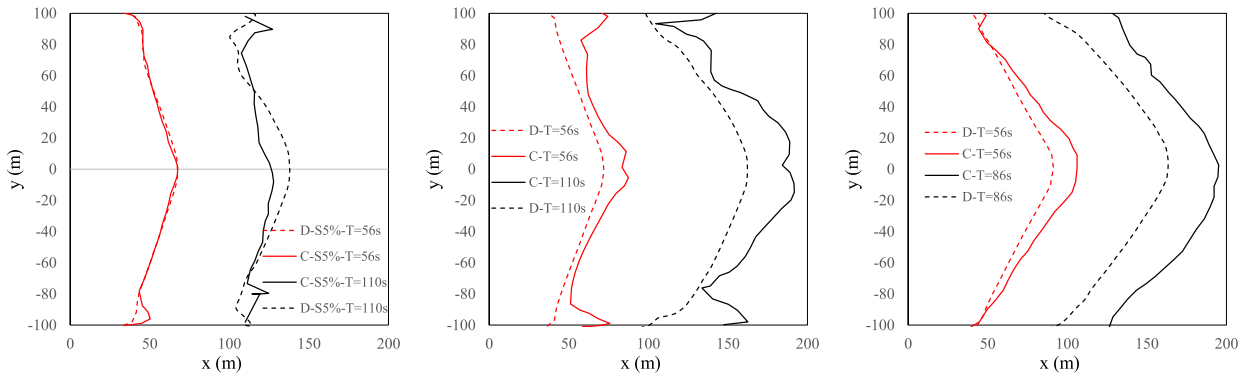

(a) S=5% (b) S=15% (c) S=30%

Fig. 6. Fire perimeter as predicted by coupled (C) and decoupled (D) FDS-LS at three different times for three different slopes.

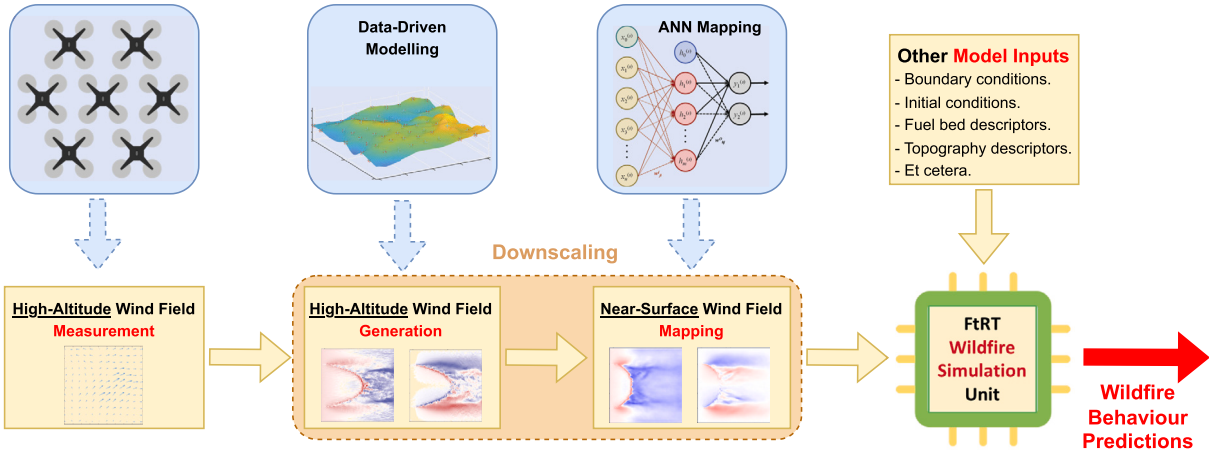

Fig. 7. System-level description of the proposed methodology to enhance wildfire model predictions using near-surface wind fields approximated from measurements at a high altitude (specifically, at flight height).

originally proposed with decoupled wildfire models in mind. Nonetheless, it may be applied to coupled models as well, potentially using data assimilation to correct the wind field predicted by the model. A top-level description of the methodology is shown in Fig. 7 and summarised below:

1. A swarm of UAVs measure wind velocity at different 2D locations at flight height, at a given time $t = t_i$.
2. The measured wind velocities are used to generate a high-resolution wind field using a data-driven super-resolution approach.
3. The high-resolution wind field at flight height is used to approximate the near-surface wind field by means of a mapping method such as a neural network.
4. The downscaled near-surface wind field is fed into the FtRT simulator, which forecasts the fire propagation for the desired predictive horizon ($\mathcal{T}$). Thus, the fire propagation is simulated in the interval $\left(t_i, t_i + \mathcal{T}\right]$.
5. Once the time increment (Δt) for updates has elapsed, swarm-based measurements are re-taken at $t_{i+1} = t_i + \Delta t$ and the process is repeated to predict the fire propagation in the $\left(t_{i+1}, t_{i+1} + \mathcal{T}\right]$ interval. Thus, the predictive horizon moves forward by $\Delta t \ll \mathcal{T}$.

The fire propagation forecast during the predictive horizon ($\mathcal{T}$) can be used to assist firefighting operations, with surface wind remaining frozen during this time. Nonetheless, the outputs of the simulator after every Δt, together with the updated near-surface wind field at that time, comprise the inputs into the simulator to forecast the fire propagation during the next predictive horizon.

Although it may be often infeasible to have a swarm of UAVs airborne solely to take wind measurements, equipping them with appropriate sensors (and possibly effectors) would enable the swarm to perform more than one task simultaneously. For example, consider the swarm of self-organising drones proposed by Innocente and Grasso [7] or the drone fleet system proposed by Ausonio et al. [31], which could easily be taking imagery and measuring environmental variables like wind, temperature, or pressure whilst engaged in fire suppression and/or monitoring activities. A bird's eye view of an envisioned wildfire emergency response system is shown in Fig. 8, which assimilates the methodology to enhance wildfire model predictions proposed in this paper and shown in Fig. 7.

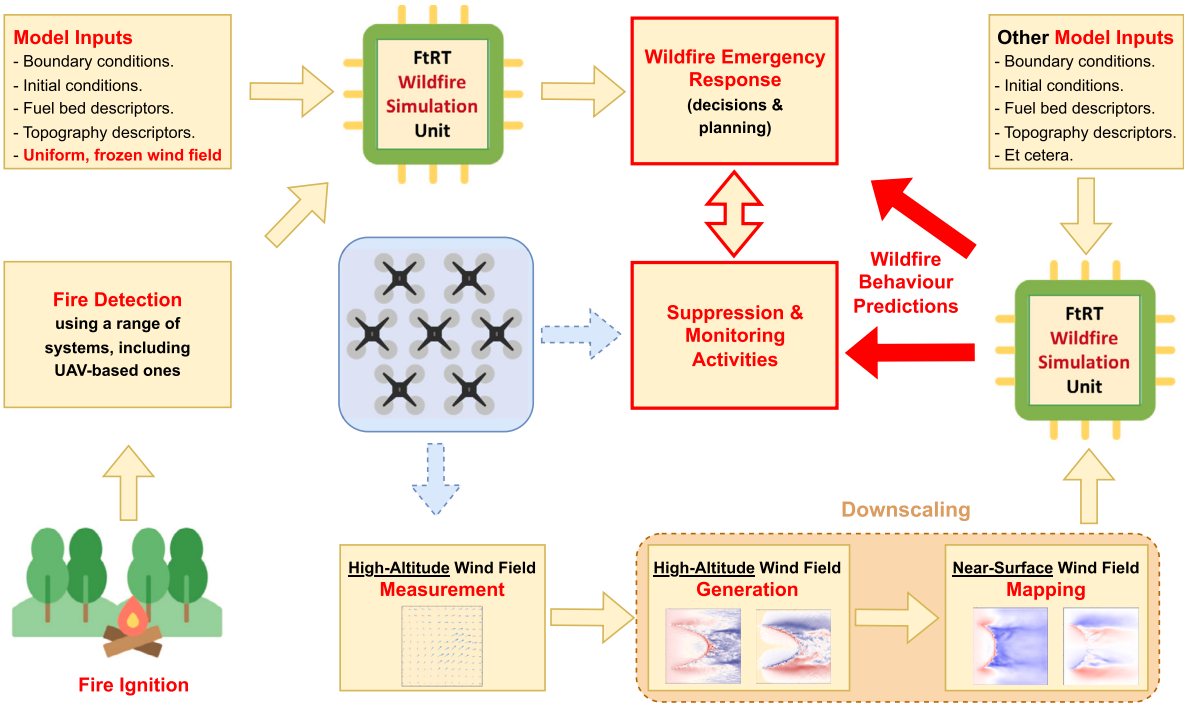

Fig. 8. Bird's eye view of an envisioned wildfire emergency response system empowered by UAV swarms, which assimilates the proposed methodology shown in Fig. 7 to enhance fire propagation model predictions. For the UAV swarm undertaking suppression activities, please refer to [7,31].

Evidently, the smaller the Δt between measurements the better, as the wind is kept frozen for shorter periods of time. A range of simulations is carried out in Section 5.1 to study the effect of Δt on a flat grassland covered with a uniform fuel bed. Since actual wind measurements are *certain to be uncertain*, Section 5.2 provides an initial attempt at studying the effect of uncertainty on the wildfire model predictions.

4.2. Swarm-based wind field measurement

Current technology to measure wind velocities includes traditional methods like cup anemometers and weather balloons, and more modern ultrasonic and laser-based systems. Conventional measurements above 60 m AGL require the building of costly towers, which motivates the use of alternative technologies such as *drone-mounted wind LiDARs* [24] and *drone-mounted ultrasonic anemometers* [25]. Unlike mechanical anemometers, wind LiDARs measure the wind speed remotely, without direct contact with the atmosphere [44]. There are two types of Doppler wind LiDARs: (*i*) *continuous wave LiDARs* emit a high-frequency concentrated laser beam at the specified location for ranges of 10 m to 250 m AGL, whilst (*ii*) *pulsed LiDARs* generate a volley of low-frequency laser pulses so that wind velocity can be measured along a line at different locations simultaneously for ranges of 50 m to 10 km AGL [24].

Airborne atmospheric measurements may be taken using fixed-wing or rotor-based drones. The former are especially suitable for long-range and long-endurance flights, as they can reach considerably higher lift-to-drag (L/D) ratios. This translates to much lower thrust requirements than similar-sized rotor-based drones and, therefore, to longer endurance [25]. On the other hand, rotor-based drones do not require a runway to take off; they offer greater manoeuvrability and have the ability to hover [22]. Measurements can be taken (*i*) *indirectly* by evaluating the drone response to the surrounding wind field [45], or (*ii*) *directly* by means of dedicated sensors [23,25]. The most common sensors used in UAVs include pitot tubes and multi-hole pressure probes [46], mechanical and sonic anemometers [45,47], and LiDAR systems [24]. Wind speed measurement errors have been reported to be around 3% under horizontal inflows and ideally levelled conditions [45,48], around 10–20% for harder situations [49,50], and in the range of 20–50% when mounted on quadrotors [45].

Wetz et al. [23] proposed using multiple UAVs for synchronised wind velocity measurements in the atmospheric boundary layer (ABL), where a small swarm of 10 UAVs operates simultaneously to provide the spatial distribution in the vicinity of wind turbines. Their algorithm estimates wind velocity making use of the principle of aerodynamic drag and related quadcopter dynamics.

Since the airflow around a wildfire is highly turbulent and hot, it may be argued that flying drones in those regions present a high risk of failure, especially for small-sized UAVs [51]. In order for the latter to cope with hazardous and all-weather conditions, there is substantial work being carried out on the design of more robust controllers [52] and of more resilient structures and materials [51,53,54].

This paper proposes the use of UAV swarms to periodically take multiple, simultaneous, real-time wind velocity measurements which will be subsequently used to construct the wind field to be fed into a wildfire propagation model. This removes the need to

couple a wind model, and could be performed while carrying out other fire emergency response tasks such as fire perimeter monitoring, fire suppression, or evacuation assistance. UAVs are particularly suitable because they do not require preinstalled infrastructure, whilst they can carry a range of sensors, reach hard-to-access areas with ease, and keep human firefighters further away from danger. In turn, swarms are particularly suitable because they allow for multiple simultaneous measurements to help capture the general trend of the wind field. The specific UAV and sensor technologies to take the measurements and the swarming behaviour are beyond the scope of this paper.

4.3. Wind field downscaling

The accurate wind field estimation is of great importance in numerous applications. However, numerical weather models require powerful computing resources, which restricts the feasibility of fine-scale and high-resolution forecasts [18]. This has led to coarse-scale weather models often being employed in wildfire decision-support systems. A domain-average wind field may be constructed using such models, usually in the form of uniform wind fields [55].

Downscaling methods avoid costly high-resolution simulations across large geographic scales by inferring high-resolution from low-resolution data [18]. They may be either *dynamic* or *statistical* [56], with dynamic methods falling into either the *prognostic* or the *diagnostic* categories.

Prognostic methods such as those employed in numerical weather forecasting solve mass, momentum, energy, and moisture conservation equations, and advance in time. They often include detailed models for the dynamics of boundary layers, land–atmosphere interactions, radiation, thermodynamics, and cloud processes. Therefore, these methods demand a substantial amount of computational power, have complicated initial and boundary conditions, and require highly skilled operators for their use [55,57].

Alternatively, statistical downscaling makes use of results from large-scale simulations with coarse spatial resolution (*predictor data*) to derive predictions at smaller scales with fine resolution (*predictand data*). These methods are trained on a given set of predictor–predictand data pairs to learn the correlations between coarse and fine data [18]. Machine Learning (ML) and Deep Learning (DL) techniques are particularly useful in this domain. Specifically, Convolutional Neural Networks (CNNs) have found vast applications in downscaling atmospheric parameters such as wind fields for both, the construction of the wind field at a high altitude from point measurements [58] and the improvement of the wind field resolution [18,59,60]. Since the aim of the proposed methodology is to enhance predictions made by FtRT simulations, statistical downscaling methods are preferred. They can be trained in advance and be efficiently evaluated in real-time under operational conditions.

Since this paper aims to demonstrate how the proposed methodology enhances FtRT decoupled model predictions by periodically feeding it with multiple wind measurements, the development and training of a specific statistical downscaling method is beyond its scope. Therefore, wind velocities are not actually measured and downscaled in this paper but extracted from three-dimensional (3D) high-fidelity physics-based Large Eddy Simulations in FDS. The *downscaling module* within the proposed system will be presented in detail in an upcoming paper devoted specifically to it.

5. Simulations and analysis of results

5.1. Enhancing wildfire model predictions

A series of 3D grassland fire propagation simulations are performed using FDS-LPM and FDS-BFM, with the resulting wind field extracted at different time-steps and provided to FireProM-F as if it were the output of the wind field *downscaling module* in Fig. 7. The effect of feeding the decoupled wildfire propagation model with the wind field is studied for a range of time intervals between consecutive “measurement” updates (Δt).

Thus, the CSIRO C064 experiment is simulated using FDS-LPM and FDS-BFM with cell sizes of $1\times1\times1$ m^3 and $0.5\times0.5\times0.5$ m^3. Fig. 9 shows the simulated wildfire at three time instants using $0.5\times0.5\times0.5$ m^3 cells, with both models predicting similar RoS despite their different representations of the fuel bed. Since both simulators rely on LES to model turbulence, they include stochasticity and therefore predict fire perimeters which are not perfectly symmetrical. This is more noticeable on the flanks of the fire. Given that FDS-LPM is expected to be a more realistic representation of the real phenomena, and also that it appears to predict slightly more symmetrical fire perimeters, the wind “measurements” for the following experiments are extracted from the wind field generated by this model.

In order to investigate the effect of the time increment between wind measurements, the CSIRO C064 experiment is simulated with FireProM-F for 120 s and for five different values of Δt. The specific settings are provided in Table 2, whilst the temperature distributions are shown in Fig. 10 at three points in time: 27 s, 53 s, and 100 s after ignition. In the first case, there is a single wind field input at the beginning of the simulation, which effectively means that the wind is frozen. The other cases consider decreasing values of Δt between measurements (and therefore between wind field inputs into the wildfire model) in order to somewhat account for the fire-induced wind without having to couple a computationally expensive wind model. For example, there are four wind field inputs into FireProM-F during the 120 s simulation for $\Delta t = 30$ s.

The results for a uniform, frozen wind field are shown in Figs. 10 (a), (b) and (c), providing a baseline against which to evaluate the effect of Δt. It can be observed that the fire front resulting from using a frozen wind field, thus disregarding the fire-induced wind, has a pointy shape that differs from the shapes displayed both in the field experiments and in the FDS-LPM simulations (see Fig. 9). Conversely, the proposed periodic update of the wind field constructed from measurements every Δt leads to more realistic shapes of the fire front. Comparing Figs. 9 and 10 at $t = 27$ s, it is clear that the shapes of the fire front are more similar to one

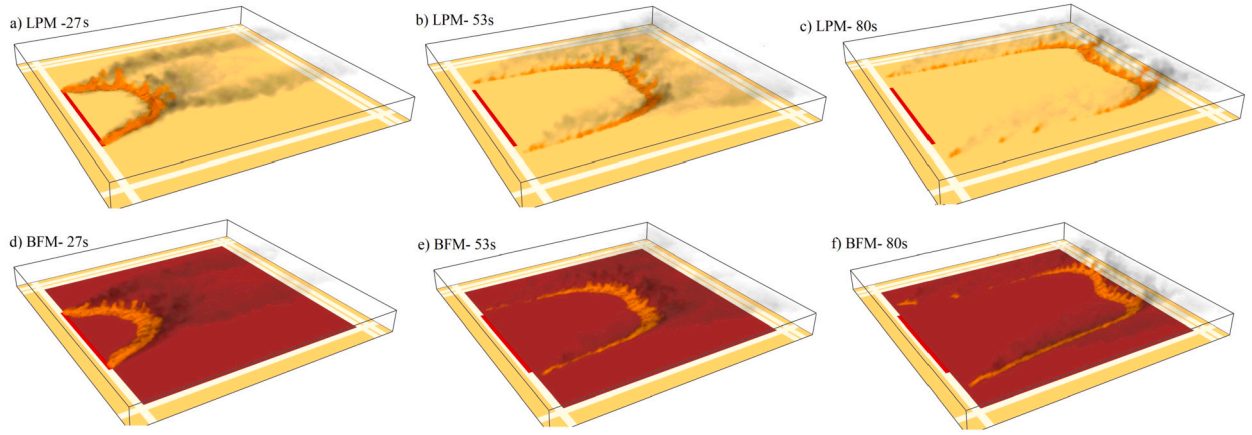

Fig. 9. Simulated wildfire propagation at three points in time for CSIRO C064 experiment using FDS-LPM (top) and FDS-BFM (bottom) and $0.5 \times 0.5 \times 0.5$ m^3 cells.

Table 2
Wind field inputs/updates during a 120 s simulation of wildfire propagation for different values of the time increment Δt.

No. Wind Inputs	Δt (s)	Wind Input Times (s)
1	120	0
4	30	0, 30, 60, 90
6	20	0, 20, 40, 60, 80, 100
12	10	0, 10, 20, 30, 40, 50, ..., 100, 110
24	5	0, 5, 10, 15, 20, ..., 110, 115

another for smaller values of Δt (i.e. for higher frequencies of updates). For larger Δt, the fire front reaches the counter-rotating vortex pairs which form downstream before the next update (not shown here), affecting the formation of the fire front and the pace of its propagation. Therefore, reducing Δt, consequently increasing the frequency of wind field updates, may prevent or reduce the effect of this numerical (artificial) phenomenon. Furthermore, a visual comparison of Figs. 10 (g), (h) and (i) ($\Delta t = 20$ s), Figs. 10 (j), (k) and (l) ($\Delta t = 10$ s), and Figs. 10 (m), (n) and (o) ($\Delta t = 5$ s) suggests that reducing Δt results in slightly faster propagation of the fire (i.e. higher RoS).

It is important to note that FireProM-F is deterministic. Therefore, the fire perimeter is symmetric for uniform wind and uniformly distributed fuel, as shown in Figs. 10 (a), (b) and (c). The asymmetries in the remaining figures, in which the wind field is updated during the simulation, are due to FDS relying on LES to model turbulence, therefore introducing stochasticity. In fact, the fire perimeters predicted by FDS-LPM and FDS-BFM in Fig. 9 are also asymmetric. Recall that the wind field modelled by FDS-LPM is taken here as ground truth to represent actual measurements, and are then provided to FireProM-F to enhance its predictions. Furthermore, a wind field extracted from the simulations corresponds to a specific point in time, which means that it is not time-averaged and is therefore affected by the oscillations of the dynamic combustion phase. This also contributes, albeit to a lesser extent, to the asymmetries observed in the simulated fire perimeters.

Fig. 11 shows the simulated fire perimeter corresponding to the CSIRO C064 experiment at three points in time predicted by FireProM-F enhanced by wind field inputs derived from wind measurements every $\Delta t = 5$ s (red dotted lines). These predictions are in agreement with actual field measurements shown in the figure by black markers.

Fig. 12 shows the burned area at three points in time after ignition: experimentally measured; predicted by FDS-LPM (coupled); predicted by FireProM-F (decoupled) with frozen and uniform wind; and predicted by FireProM-F (decoupled) enhanced by wind field inputs derived from wind measurements with different values of Δt. As can be observed, the burned area simulated by FDS-LPM is larger than the one experimentally measured. One source of this significant discrepancy is that *atmospheric wind* (i.e. disregarding fire-induced wind) velocities are variable both in intensity and direction during field experiments, whereas they are constant during simulations. It can also be observed that the burned area predicted by the enhanced FireProM-F is closer to the one predicted by FDS-LPM than it is to the one experimentally measured. This makes sense since the wind fields provided to FireProM-F were extracted from FDS-LPM simulations. In fact, the smaller the Δt the better the agreement between them. In contrast, the burned area predicted by the decoupled Fire-ProM-F is closer to the one experimentally measured.

With regards to the computational effort, it is worth mentioning that simulating wildfire propagation within a 100×100 m^2 area discretised into 10,000 2D cells is performed up to 3.33 times faster than real time. That is to say that 1 min of wildfire propagation is simulated in 18 s on a single-core CPU. This may be reduced by orders of magnitude if implemented on parallel processing frameworks, which makes this approach especially suitable for operational settings.

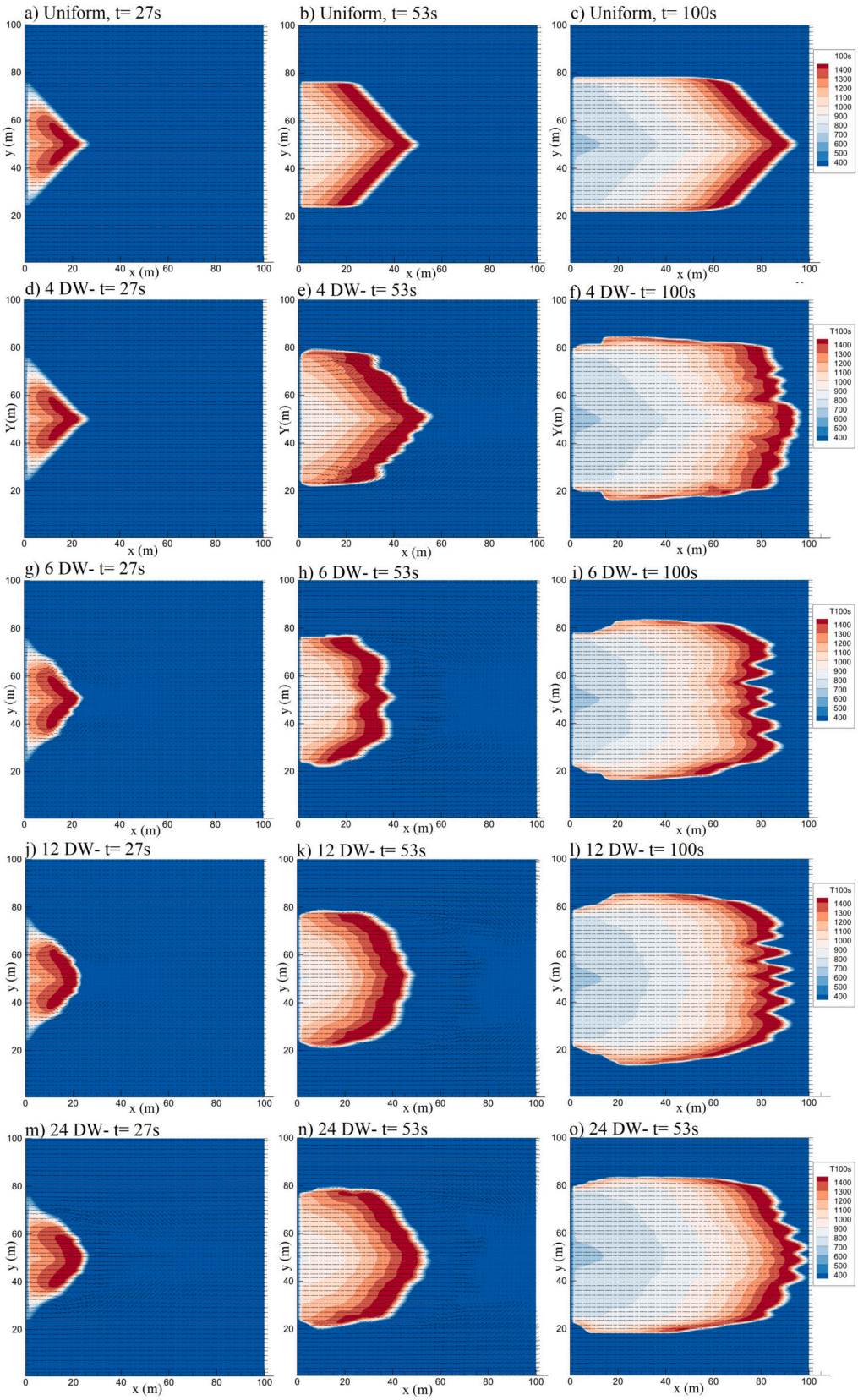

Fig. 10. Temperature profile at three points in time from a 120 s simulation of the CSIRO C064 experiment by FireProM-F (decoupled) enhanced by wind fields inputs derived from wind measurements with update intervals (Δt) as in Table 2. Note that "X DW" stands for "X dynamic wind field inputs during the simulation".

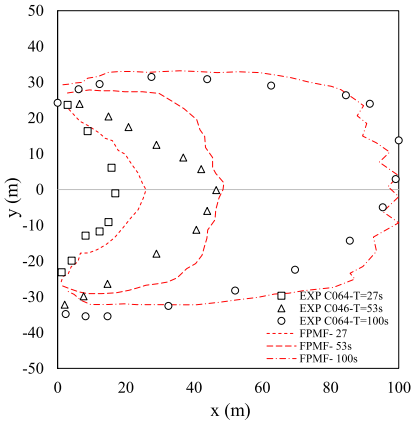

Fig. 11. Three time instances of the CSIRO C064 experiment, where actual measurements are shown by black markers whilst the fire perimeter predicted by FireProM-F enhanced by wind field inputs derived from wind measurements every $\Delta t = 5$ s is shown by red dotted lines.

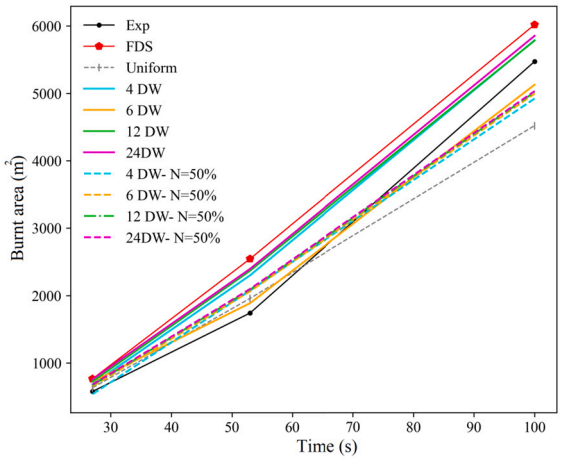

Fig. 12. Burned area of CSIRO C064 experiment at three time instances after ignition: experimentally measured, predicted by FDS-LPM (coupled), predicted by FireProM-F (decoupled) with frozen wind, and predicted by FireProM-F (decoupled) enhanced by wind field inputs derived from wind measurements with different update intervals (Δt). Note that "X DW" stands for "X dynamic wind field inputs during the simulation", whilst the percentage refers to Gaussian noise.

5.2. Effect of wind measurement uncertainty

Wind speed measurement errors have been reported to be in the range of 20–50% when mounted on quadrotors [45]. In order to perform a preliminary study of the effect of these measurement uncertainties on the simulated wildfire propagation, two scenarios are considered: (*i*) 30% and (*ii*) 50% Gaussian noise added to the "measurements". In other words, noise is sampled from a normal distribution with standard deviation equal to 30% and 50% of the wind velocity, respectively. Figs. 13 and 14 show the temperature distribution at three points in time after ignition returned by FireProM-F simulating the CSIRO C064 experiment with noisy wind field inputs every 30 s and 10 s, respectively. As can be observed, the general shape of the burned area remains despite the noise, with the fire front displaying a more defined shape and faster propagation (higher RoS) for lower levels of noise (see also Fig. 10). This is in agreement with the burned area decreasing when 50% noise is added to the "measurements" in Fig. 12.

6. Conclusions

The prediction accuracy of wildfire propagation models is influenced by numerous factors such as the fidelity of the fuel descriptors, adequate initial and boundary conditions, the coupling with atmospheric models, and the coupling with wind models such as Navier-Stokes equations to account for the fire–wind interaction. This paper focused on the latter. Wildfire models which include wind in their governing equations but are not coupled with a wind model are referred to here as *decoupled wildfire propagation models*. This means that fire propagation is affected by atmospheric wind, yet the effect of the fire on the wind field is neglected.

This paper proposed a method for enhancing the prediction accuracy of a wildfire propagation model by periodically providing it with wind fields constructed from wind measurements. In the proposed method, measurements are to be taken by UAV swarms. However, wind velocities were extracted from high-fidelity physics-based simulations instead. In this proof of concept, the aim was

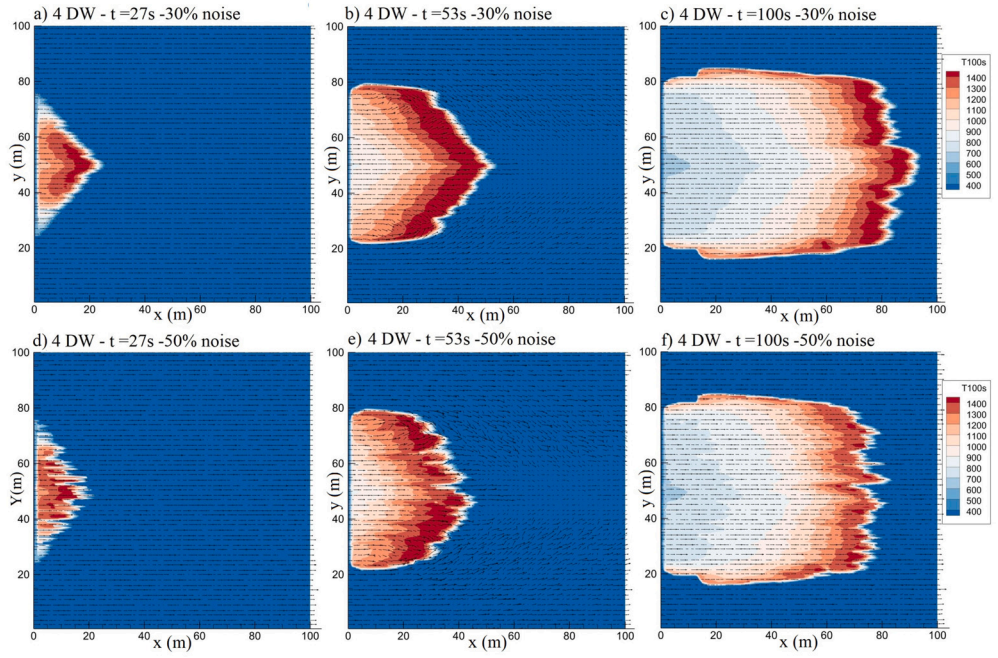

Fig. 13. Temperature profile at three points in time from a 120 s simulation of the CSIRO C064 experiment by FireProM-F (decoupled) enhanced by wind fields inputs with 30% (top) and 50% (bottom) Gaussian noise with update interval $\Delta t = 30$ s. Note that "X DW" stands for "X dynamic wind field inputs during the simulation".

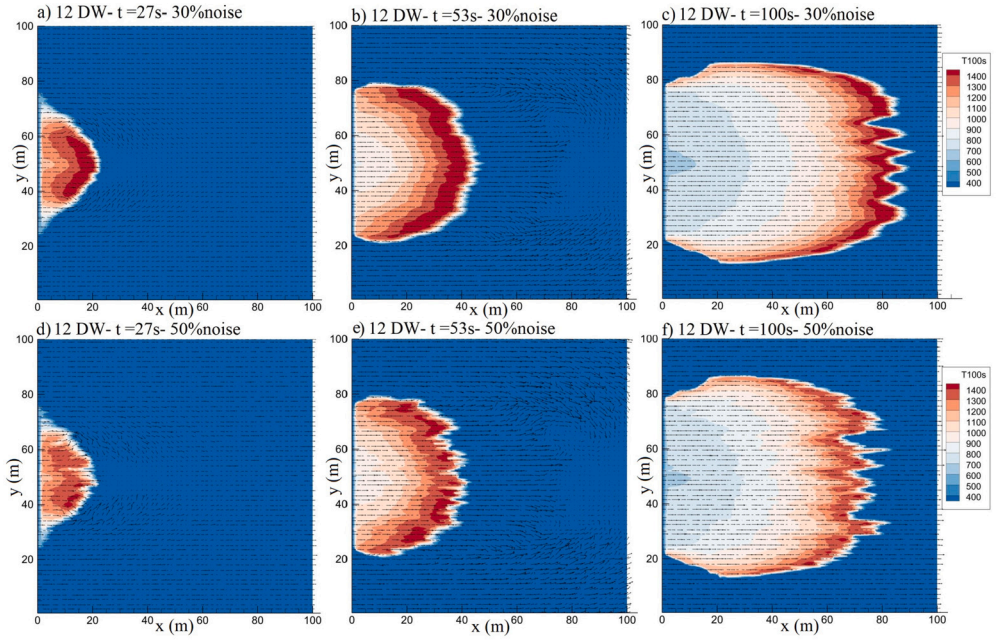

Fig. 14. Temperature profile at three points in time from a 120 s simulation of the CSIRO C064 experiment by FireProM-F (decoupled) enhanced by wind fields inputs with 30% (top) and 50% (bottom) Gaussian noise with update interval $\Delta t = 10$ s. Note that "X DW" stands for "X dynamic wind field inputs during the simulation".

to focus on the feasibility of accounting for the effect of the fire on the wind field by periodically feeding the latter into a decoupled fire model instead of coupling a wind model. Positioning uncertainties, measurement uncertainties, measurements distribution, and the data-driven models to construct the wind field are left for future work. Thus, fire–wind interactions were accounted for without resolving computationally expensive mass and momentum balance equations. Therefore, decoupled wildfire propagation model predictions were enhanced while still retaining the ability to perform faster-than-real-time (FtRT) simulations to assist wildfire emergency response operations. Originally targeting *decoupled models*, the proposed method could also enhance predictions of *coupled* models via data assimilation. It is model agnostic, and hence may be integrated with any wildfire propagation model.

The CSIRO C064 and F19 field experiments were simulated under different conditions and using a range of wildfire propagation models: (*i*) FDS-LPM (CFD simulator); (*ii*) FDS-LS (level set model within FDS); (*iii*) FireProM-F (2D physics-based simulator) with frozen wind field; and (*iv*) FireProM-F enhanced by periodic inputs of wind fields.

Simulations performed using coupled and decoupled FDS-LS showed that coupling leads to higher RoS, closer to the values reported from field experiments. The difference in RoS increases with increasing atmospheric horizontal reference wind speeds and with higher terrain positive slopes. This is presumed to be due to coupled models being able to better capture fire-induced convective wind patterns upslope (downstream). Furthermore, the coupling of a turbulent wind model results, unsurprisingly, in the predicted fire perimeter being less smooth.

In order to study the effect of the proposed method to enhance decoupled wildfire propagation model predictions, a series of wind fields generated by FDS-LPM were used to stand for actual wind measurements. FireProM-F was used as an example of a decoupled FtRT simulator whose predictions are to be enhanced by the proposed method. Thus, a series of fire propagation simulations were performed periodically providing the model with "measured" wind fields. The resulting fire fronts and burned areas were then compared against those predicted by CFD simulations (FDS-LPM) representing the ground truth. This makes sense because they had provided the wind fields as a surrogate of the measured ones. Results demonstrate that the enhanced FireProM-F makes more accurate predictions than the plain version, and that the higher update frequencies, $\Delta t = 10$ s and $\Delta t = 5$ s, predict burned areas very similar to the ground truth. Furthermore, the fire front predicted by the enhanced FireProM-F was shown to track the ones observed in the field experiments accurately.

Since wind was not measured in the field for these experiments but extracted from FDS-LPM simulations, Gaussian noise was added to perform a preliminary study of the effect of measurement uncertainty. Results showed that the general shape of the burned area remains more or less the same when adding 30%–50% noise, with the fire front displaying a less smooth shape and slower propagation as noise increases.

Thus, the proposed method has been shown to enhance decoupled wildfire propagation model predictions, as it had been hypothesised. Still, this is a conceptual framework and considerable work remains to be done to bring the concept closer to deployment. The next steps in our research are the design of the wind downscaling mechanism, and the investigation of the performance of the proposed methodology when measurements are less regular; e.g. when the swarm is performing other activities while taking measurements.

CRediT authorship contribution statement

Mohammad: Conceptualization, Methodology, Software, Writing, Investigation, Visualization. Mauro Sebastián Innocente: Conceptualization, Methodology, Software, Writing, Supervision, Resources, Visualization.

Declaration of competing interest

The authors declare that they have no known competing financial interests or personal relationships that could have appeared to influence the work reported in this paper.

Data availability

Data and in-house codes will be made available in the AVAILAB's GitHub account. References provide information on where to find data and software by others.

References

[1] P. Jain, S.C. Coogan, S.G. Subramanian, M. Crowley, S. Taylor, M.D. Flannigan, A review of machine learning applications in wildfire science and management, Environ. Rev. 28 (4) (2020) 478–505, https://doi.org/10.1139/er-2020-0019.

[2] B.E. Potter, Atmospheric interactions with wildland fire behaviour - I. Basic surface interactions, vertical profiles and synoptic structures, Int. J. Wildland Fire 21 (7) (2012) 779, https://doi.org/10.1071/wf11128.

[3] H.T. Gisborne, Measuring forest-fire danger in northern Idaho, Tech. Rep. 29, Rocky Mountain Research Station, 1928, https://www.fs.usda.gov/research/treesearch/48904.

[4] A.L. Sullivan, Wildland surface fire spread modelling, 1990 - 2007. 1: physical and quasi-physical models, Int. J. Wildland Fire 18 (4) (2009) 349, https://doi.org/10.1071/wf06143.

[5] A.L. Sullivan, Wildland surface fire spread modelling, 1990 - 2007. 2: empirical and quasi-empirical models, Int. J. Wildland Fire 18 (4) (2009) 369, https://doi.org/10.1071/wf06142.

[6] A.L. Sullivan, Wildland surface fire spread modelling, 1990 - 2007. 3: simulation and mathematical analogue models, Int. J. Wildland Fire 18 (4) (2009) 387, https://doi.org/10.1071/wf06144.

[7] M.S. Innocente, P. Grasso, Self-organising swarms of firefighting drones: harnessing the power of collective intelligence in decentralised multi-robot systems, J. Comput. Sci. 34 (2019) 80–101, https://doi.org/10.1016/j.jocs.2019.04.009.

[8] P. Grasso, M.S. Innocente, Physics-based model of wildfire propagation towards faster-than-real-time simulations, Comput. Math. Appl. 80 (5) (2020) 790–808, https://doi.org/10.1016/j.camwa.2020.05.009.

[9] A. Bakhshaii, E. Johnson, A review of a new generation of wildfire–atmosphere modeling, Can. J. For. Res. 49 (6) (2019) 565–574, https://doi.org/10.1139/cjfr-2018-0138.

[10] M.A. Finney, FARSITE: Fire area simulator-model development and evaluation, Tech. Rep. RMRS-RP-4, Revised 2004, U.S. Department of Agriculture, Forest Service, Rocky Mountain Research Station, Ogden, UT, 1998.

[11] P. Grasso, M.S. Innocente, A two-dimensional reaction- advection- diffusion model of the spread of fire in wildlands, in: Advances in Forest Fire Research, 2018.

[12] C.E. VanWagner, Forest fire research–hindsight and foresight, in: Proceedings of the Symposium on Wildland Fire, U.S. Department of Agriculture, Forest Service, Pacific Southwest Forest and Range Experiment Station, 1987.
[13] W. Mell, M.A. Jenkins, J. Gould, P. Cheney, A physics-based approach to modelling grassland fires, Int. J. Wildland Fire 16 (1) (2007) 1, https://doi.org/10.1071/wf06002.
[14] R.R. Linn, J.M. Reisner, J. Colman, J. Winterkamp, Studying wildfire behavior using FIRETEC, Int. J. Wildland Fire 11 (2002) 233–246, https://doi.org/10.1071/WF02007.
[15] J.L. Coen, M. Cameron, J. Michalakes, E.G. Patton, P.J. Riggan, K.M. Yedinak, WRF-fire: coupled weather–wildland fire modeling with the weather research and forecasting model, J. Appl. Meteorol. Climatol. 52 (1) (2013) 16–38, https://doi.org/10.1175/jamc-d-12-023.1.
[16] A.M.G. Lopes, L.M. Ribeiro, D.X. Viegas, J.R. Raposo, Effect of two-way coupling on the calculation of forest fire spread: model development, Int. J. Wildland Fire 26 (9) (2017) 829, https://doi.org/10.1071/wf16045.
[17] M. Tavakol Sadrabadi, M.S. Innocente, E. Gkanas, I. Papagiannis, Comparison of the effect of one-way and two-way fire-wind coupling on the modelling of wildland fire propagation dynamics, in: Advances in Forest Fire Research 2022, Imprensa da Universidade de Coimbra, 2022, pp. 115–121.
[18] K. Höhlein, M. Kern, T. Hewson, R. Westermann, A comparative study of convolutional neural network models for wind field downscaling, J. Meteorol. Appl. 27 (6) (2020) e1961, https://doi.org/10.1002/met.1961.
[19] M.A. Akhloufi, A. Couturier, N.A. Castro, Unmanned aerial vehicles for wildland fires: sensing, perception, cooperation and assistance, Drones 5 (1) (2021) 15, https://doi.org/10.3390/drones5010015.
[20] B.Y. Lattimer, X. Huang, M.A. Delichatsios, Y.A. Levendis, K. Kochersberger, S. Manzello, P. Frank, T. Jones, J. Salvador, C. Delgado, E. Angelats, M.E. Parés, D. Martín, S. McAllister, S. Suzuki, Use of unmanned aerial systems in outdoor firefighting, Fire Technol. (2023), https://doi.org/10.1007/s10694-023-01437-0.
[21] R.S. Allison, J.M. Johnston, G. Craig, S. Jennings, Airborne optical and thermal remote sensing for wildfire detection and monitoring, Sensors 16 (8) (2016), https://doi.org/10.3390/s16081310, https://www.mdpi.com/1424-8220/16/8/1310.
[22] K. Sasaki, M. Inoue, T. Shimura, M. Iguchi, In situ, rotor-based drone measurement of wind vector and aerosol concentration in volcanic areas, Atmosphere 12 (3) (2021), https://doi.org/10.3390/atmos12030376, https://www.mdpi.com/2073-4433/12/3/376.
[23] T. Wetz, N. Wildmann, F. Beyrich, Distributed wind measurements with multiple quadrotor unmanned aerial vehicles in the atmospheric boundary layer, Atmos. Meas. Tech. 14 (5) (2021) 3795–3814, https://doi.org/10.5194/amt-14-3795-2021.
[24] N. Vasiljević, M. Harris, A. Tegtmeier Pedersen, G. Rolighed Thorsen, M. Pitter, J. Harris, K. Bajpai, M. Courtney, Wind sensing with drone-mounted wind LiDARs: proof of concept, Atmos. Meas. Tech. 13 (2) (2020) 521–536, https://doi.org/10.5194/amt-13-521-2020.
[25] W. Thielicke, W. Hübert, U. Müller, M. Eggert, P. Wilhelm, Towards accurate and practical drone-based wind measurements with an ultrasonic anemometer, Atmos. Meas. Tech. 14 (2) (2021) 1303–1318, https://doi.org/10.5194/amt-14-1303-2021.
[26] A. Viseras, M. Meissner, J. Marchal, Wildfire front monitoring with multiple UAVs using deep Q-learning, IEEE Access (2021) 1, https://doi.org/10.1109/ACCESS.2021.3055651.
[27] F.A. Hossain, Y.M. Zhang, M.A. Tonima, Forest fire flame and smoke detection from UAV-captured images using fire-specific color features and multi-color space local binary pattern, J. Unmanned Veh. Syst. 8 (4) (2020) 285–309, https://doi.org/10.1139/juvs-2020-0009.
[28] S. Sudhakar, V. Vijayakumar, C. Sathiya Kumar, V. Priya, L. Ravi, V. Subramaniyaswamy, Unmanned aerial vehicle (UAV) based forest fire detection and monitoring for reducing false alarms in forest-fires, Comput. Commun. 149 (2020) 1–16, https://doi.org/10.1016/j.comcom.2019.10.007.
[29] H. Qin, J.Q. Cui, J. Li, Y. Bi, M. Lan, M. Shan, W. Liu, K. Wang, F. Lin, Y.F. Zhang, B.M. Chen, Design and implementation of an unmanned aerial vehicle for autonomous firefighting missions, in: 2016 12th IEEE International Conference on Control and Automation (ICCA), 2016, pp. 62–67.
[30] M.S. Innocente, P. Grasso, Swarms of autonomous drones self-organised to fight the spread of wildfires, in: Proceedings of the GEOSAFE Workshop on Robust Solutions for Fire Fighting, vol. 2146, 2018, https://ceur-ws.org/Vol-2146/paper83.pdf.
[31] E. Ausonio, P. Bagnerini, M. Ghio, Drone swarms in fire suppression activities: a conceptual framework, Drones 5 (1) (2021), https://doi.org/10.3390/drones5010017, https://www.mdpi.com/2504-446X/5/1/17.
[32] K. McGrattan, R. McDermott, S. Hostikka, J. Floyd, Fire dynamics simulator user's guide, NIST Special Publication 1019-5, National Institute of Standards and Technology (NIST), Maryland, USA, 2019.
[33] M. Vanella, K. McGrattan, R. McDermott, G. Forney, W. Mell, E. Gissi, P. Fiorucci, A multi-fidelity framework for wildland fire behavior simulations over complex terrain, Atmosphere 12 (2) (2021) 273, https://doi.org/10.3390/atmos12020273, https://www.mdpi.com/2073-4433/12/2/273.
[34] A.S. Bova, W.E. Mell, C.M. Hoffman, A comparison of level set and marker methods for the simulation of wildland fire front propagation, Int. J. Wildland Fire 25 (2) (2016) 229–241, https://doi.org/10.1071/WF13178.
[35] P.L. Andrews, Modeling wind adjustment factor and midflame wind speed for Rothermel's surface fire spread model, Tech. Rep. RMRS-GTR-266, U.S. Department of Agriculture, Forest Service, Rocky Mountain Research Station, Fort Collins, CO, 2012.
[36] B.J. Mcbride, S. Gordon, M.A. Reno, Coefficients for calculating thermodynamic and transport properties of individual species, Tech. Rep., NASA, 1993.
[37] N. Cheney, J. Gould, W. Catchpole, The influence of fuel, weather and fire shape variables on fire-spread in grasslands, Int. J. Wildland Fire 3 (1) (1993) 31–44, https://doi.org/10.1071/WF9930031, https://www.publish.csiro.au/paper/WF9930031.
[38] N.P. Cheney, J. Gould, W.R. Catchpole, Prediction of fire spread in grasslands, Int. J. Wildland Fire 8 (1998) 1–13, https://doi.org/10.1071/WF9980001.
[39] B.W. Butler, W.R. Anderson, E.A. Catchpole, Influence of slope on fire spread rate, in: The Fire Environment–Innovations, Management, and Policy Conference, U.S. Department of Agriculture, Forest Service, Rocky Mountain Research Station, Fort Collins, CO, 2007.
[40] A.G. McArthur, Australia. Weather and Grassland Fire Behaviour, Forestry and Timber Bureau, Canberra, 1966.
[41] M.A.F. Torben, P. Grumstrup, Sara S. McAllister, Qualitative flow visualization of flame attachment on slopes, in: 10th U. S. National Combustion Meeting, 2017.
[42] M. Li, Z. Shu, S. Geng, G. Han, Experimental and modelling study on flame tilt angle of flame spread over jet fuel under longitudinally forced air flows, Fuel 270 (2020) 117516, https://doi.org/10.1016/j.fuel.2020.117516.
[43] F. Morandini, X. Silvani, J. luc Dupuy, A. Susset, Fire spread across a sloping fuel bed: flame dynamics and heat transfers, Combust. Flame 190 (2018) 158–170, https://doi.org/10.1016/j.combustflame.2017.11.025.
[44] M. Shangguan, J. Qiu, J. Yuan, Z. Shu, L. Zhou, H. Xia, Doppler wind LiDAR from UV to NIR: a review with case study examples, Front. Remote Sens. 2 (Mar. 2022), https://doi.org/10.3389/frsen.2021.787111.
[45] G.W. Donnell, J.A. Feight, N. Lannan, J.D. Jacob, Wind characterization using onboard IMU of sUAS, in: 2018 Atmospheric Flight Mechanics Conference, 2018.
[46] S. Prudden, A. Fisher, M. Marino, A. Mohamed, S. Watkins, G. Wild, Measuring wind with small unmanned aircraft systems, J. Wind Eng. Ind. Aerodyn. 176 (2018) 197–210, https://doi.org/10.1016/j.jweia.2018.03.029.
[47] V. Natalie, J.D. Jacob, Experimental observations of the boundary layer in varying topography with unmanned aircraft, in: AIAA Aviation 2019 Forum, 2019.
[48] R.T. Palomaki, N.T. Rose, M. van den Bossche, T.J. Sherman, S.F.J.D. Wekker, Wind estimation in the lower atmosphere using multirotor aircraft, J. Atmos. Ocean. Technol. 34 (2017) 1183–1191, https://doi.org/10.1175/JTECH-D-16-0177.1.
[49] P.J. Nolan, J.O. Pinto, J. González-Rocha, A. Jensen, C.N. Vezzi, S.C.C. Bailey, G. de Boer, C. Diehl, R. Laurence, C. Powers, H. Foroutan, S.D. Ross, D.G. Schmale, Coordinated unmanned aircraft system (UAS) and ground-based weather measurements to predict Lagrangian coherent structures (LCSs), Sensors 18 (2018), https://doi.org/10.3390/s18124448.
[50] D. Hollenbeck, G. Nunez, L.E. Christensen, Y.Q. Chen, Wind measurement and estimation with small unmanned aerial systems (sUAS) using on-board mini ultrasonic anemometers, in: 2018 International Conference on Unmanned Aircraft Systems (ICUAS), 2018, pp. 285–292.
[51] A. Sattar, L. Wang, A.A. Hoshu, S. Ansari, H. e Karar, A. Mohamed, Automatic tuning and turbulence mitigation for fixed-wing UAV with segmented control surfaces, Drones (2022), https://doi.org/10.3390/drones6100302.

[52] P.I. Renn, M. Gharib, Machine learning for flow-informed aerodynamic control in turbulent wind conditions, Commun. Eng. 1 (2022) 45, https://doi.org/10.1038/s44172-022-00046-z.
[53] D. Grant, M. Abdulrahim, R. Lind, Flight dynamics of a morphing aircraft utilizing independent multiple-joint wing sweep, Int. J. Micro Air Veh. 2 (2010) 91–106, https://doi.org/10.1260/1756-8293.2.2.91.
[54] P.F. Peña, A.R. Ragab, M.A. Luna, M.S.A. Isaac, P. Campoy, Wild Hopper: a heavy-duty UAV for day and night firefighting operations, Heliyon 8 (2022), https://doi.org/10.1016/j.heliyon.2022.e09588.
[55] J.M. Forthofer, B.W. Butler, N. Wagenbrenner, A comparison of three approaches for simulating fine-scale surface winds in support of wildland fire management: part i. model formulation and comparison against measurements, Int. J. Wildland Fire 23 (2014) 969–981, https://doi.org/10.1071/WF12089.
[56] B. Hewitson, R.G. Crane, Climate downscaling: techniques and application, Clim. Res. 7 (1996) 85–95.
[57] G.F. Homicz, Three-dimensional wind field modeling: a review, Tech. Rep., Rocky Mountain Research Station, 2002, https://www.osti.gov/biblio/801406.
[58] J. Zhang, X. Zhao, Spatiotemporal wind field prediction based on physics-informed deep learning and LiDAR measurements, Appl. Energy 288 (2021) 116641, https://doi.org/10.1016/j.apenergy.2021.116641.
[59] J. Dujardin, M. Lehning Wind-topo, Downscaling near-surface wind fields to high-resolution topography in highly complex terrain with deep learning, Q. J. R. Meteorol. Soc. 148 (2022).
[60] K. Stengel, A. Glaws, D. Hettinger, R.N. King, Adversarial super-resolution of climatological wind and solar data, Proc. Natl. Acad. Sci. 117 (2020) 16805–16815.